High-resolution temperature profiling in the Π Chamber: variability of statistical properties of temperature fluctuations

Robert Grosz[1], Kamal Kant Chandrakar[2], Raymond A. Shaw[3], Jesse C. Anderson[3], Will Cantrell[3], and Szymon P. Malinowski[1]

[1]Institute of Geophysics, Faculty of Physics, University of Warsaw, Pasteura 5, 02-293 Warsaw, Poland
[2]Mesoscale & Microscale Meteorology Laboratory, NSF National Center for Atmospheric Research, 3090 Center Green Drive, Boulder, CO 80301, USA
[3]Department of Physics, Michigan Technological University, 1400 Townsend Drive, Houghton, MI 49931, USA

Correspondence: Robert Grosz (rgrosz@fuw.edu.pl)

Abstract.

This study delves into the small-scale temperature structure inside the turbulent convection Π Chamber under three temperature differences (10 K, 15 K, and 20 K) at Rayleigh number Ra $\sim 10^9$ and Prandtl number Pr ≈ 0.7. We performed high frequency measurements (2 kHz) with the UltraFast Thermometer (UFT) at selected points along the vertical axis. The miniaturized design of the sensor featured with a resistive platinum-coated tungsten wire, 2.5 μm thick and 3 mm long, mounted on a miniature wire probe allowed for vertically undisturbed temperature profiling through the chamber's depth spanning from 8 cm above the bottom to 5 cm below the top. The collected data, consisting of 19 min and 3 min time series, were used to investigate the variability of the temperature field within the chamber, aiming to better address scientific questions related to its primary objective: understanding small-scale aerosol-cloud interactions. The analyses reveal substantial variability in both variance and skewness of temperature distributions near the top and bottom plates and in the bulk (central) region, which were linked to local thermal plume dynamics. We also identified three spectral regimes termed inertial range (slopes of $\sim -7/5$), transition range (slopes of ~ -3) and dissipative range, characterized by slopes varying ~ -7. Furthermore, the analysis showed a power law relationship between the periodicity of large-scale circulation (LSC) and the temperature difference. Notably, experimental results are in good agreement with Direct Numerical Simulations (DNS) conducted under similar thermodynamic conditions, illustrating a comparative analysis of this nature.

1 Introduction

The convection-cloud chamber, officially named the Π Chamber, represents one of the most advanced facilities for controlled experiments on cloud microphysics (Chang et al., 2016). Its design allows for reproducible and controlled measurements across a wide range of temporal scales, from minutes to days, while maintaining stationary thermodynamic forcing. It operates in two modes. The first mode utilizes static pressure reduction to simulate updrafts in the atmosphere. In the second mode, it induces Rayleigh-Bénard convection (RBC), where air in the chamber is heated from below and cooled from above. In the present study we investigate temperature fluctuations in full spectrum of scales in the chamber operating in the second mode. We focus on small-scale temperature fluctuations in a course of turbulent mixing inside the chamber, since the facility is designed for research on aerosol-cloud interactions in turbulent environment (Chandrakar et al., 2018a, b; Desai et al., 2018, 2019; Chandrakar et al., 2020; Prabhakaran et al., 2020; MacMillan et al., 2022). Unlike typical RBC experiments, the chamber includes side windows and various mounting points for microphysical instrumentation, which introduce asymmetries between the upper and lower plates. Thus the detailed (e.g. thermal) characterization of the chamber is required to evaluate how closely the flow resembles classic RBC flows. It is important to note that this study does not aim to extend beyond conventional RBC research, which often involves day-long averaging.

Atmospheric phenomena undergo non-stationary and unstable processes, making them difficult to study in real atmosphere conditions. The RBC setup used in this study provides more controllable environment than the real atmosphere but we do not push to reach the level of convergence recognized in the RB community. Nonetheless, we report statistics which can be compared to previous highly-resolved measurements within the RBC systems (du Puits et al., 2013; du Puits, 2022; du Puits, 2024).

Our work primarily focuses on understanding the small-scale and short-term variability of thermal conditions within the facility, emphasizing the importance of absolute temperature. This aspect is crucial for more comprehensive studies on aerosol interactions with water vapor and droplet growth/evaporation in a turbulent environment. However, a few selected results are presented in a non-dimensional form (see Appendix B). One recent study of particular relevance to small-scale variability is the paper by Salesky et al. (2024) on the subgrid scale scalar variance modeled in large eddy simulations over the range Ra $\sim 10^8$–10^9. Our approach was to collect high resolution (2 kHz) temperature time series using the UltraFast Thermometer (UFT) at selected locations in a vertical profile near the axis of the chamber and to perform statistical and spectral analysis investigating small-scale structure of RBC under laboratory conditions.

UltraFast Thermometers (UFTs) have been specifically designed for airborne in-cloud measurements. They resolve scales down to or even below 1 cm, effectively reaching the dissipation range. Successive models of the UFT family (Haman et al., 1997, 2001; Kumala et al., 2013) have utilized similar sensing element–a resistive platinum-coated tungsten wire, 2.5 $\mu\mathrm{m}$ thick and 5 mm long, mounted on a small vane to adapt to local airflow. In the next sensor versions (Nowak et al., 2018; Siebert et al., 2021), the vane has been removed, leading to further miniaturization of the instrument's dimensions and the implementation of a custom-built electronic system. The current iteration (UFT-2B) has undergone testing i.e. during the recent EUREC^{4}A campaign (Stevens et al., 2021). The 3 mm long sensing wire is spanned on an industry-standard miniature wire probe, allowing for easy exchange of the sensing head (see Fig. 1).

Not only small-scale fluctuations are important in their own sake, but also for understanding of changes in the LSC on distributions of mixing ratio, temperature, and supersaturation inside the cell. The established LSC period in the Π Chamber at the temperature difference of 12 K, was estimated to be $\tau_{12} \approx 72$ s (moist convection characterized by a mixing ratio of 7.55 $\mathrm{g\,kg^{-1}}$) (Anderson et al., 2021). In this paper we investigate LSC for three temperature differences (ΔT): 10 K, 15 K, and 20 K showing a variability of periodicity which can be described by the power law function.

To place our measurements in a broader context, we discuss the results from canonical RBC systems that have been conducted over the years. For comprehensive overviews of recent advancements in RBC, see the works by Fan et al. (2021) and

Figure 1. UFT-2B head sensor. A parallel to the mean flow, tungsten wire (2.5 µm thick, 3 mm long) spanned on miniature industry-standard wire probe by DANTEC®.

Lohse and Shishkina (2024), along with their references. A more detailed analyses of statistical properties of the temperature field in RBC has been explored in recent experimental (He et al., 2018; Wang et al., 2019, 2022), theoretical (Shishkina et al., 2017; Olsthoorn, 2023), and numerical (Xu et al., 2021b) studies where the authors characterized boundary layer and mixing zone of convective flows. Some investigations aimed at describing buoyant thermal plumes departing from the thermal boundary layer, contributing to the overall heat flux through LSC in a wide range of Rayleigh numbers (Ra ranging from 10^7 to 10^{14}) (Liu and Ecke, 2011; van der Poel et al., 2015; Zhu et al., 2018; Blass et al., 2021; Reiter et al., 2021; Vishnu et al., 2022; Wang et al., 2022). Large-scale convective structures have been further explored through DNS, revealing relatively fewer plumes near the sidewalls carrying large heat fluxes, contrasted with more numerous plumes near the cell axis but with weaker heat fluxes, highlighting strong intermittency in this region (Lakkaraju et al., 2012; Chillà and Schumacher, 2012; Stevens et al., 2018; Pandey et al., 2018; Krug et al., 2020; Moller et al., 2021). The simulations also demonstrated the persistence of discrete thermal structures in RBC (Sakievich et al., 2016).

The studies also examined the effects of cell dimensions, revealing the variable nature of the LSC depending on the cell's aspect ratio (Γ = width/height) (Shishkina, 2021). The aspect ratio characterizing the facility (width = 2 m, height = 1 m, Γ = 2) corresponds to a single roll with a fixed orientation and pronounced oscillations about the mean position, a result of asymmetries inside the chamber (Anderson et al., 2021) (see Fig. 2). In cases where $\Gamma \gtrsim 4$, a three-dimensional, multi-roll structure has been observed (Bailon-Cuba et al., 2010; Ahlers et al., 2022). Another aspect is the stability of the LSC as numerous analysis have proved its random reorientation and reversal in both cylindrical setups (Brown and Ahlers, 2007; Mishra et al., 2011; Wei, 2021; Xu et al., 2021a) and rectangular cells (Vasiliev et al., 2016; Foroozani et al., 2017; Wang et al., 2018; Vishnu et al., 2020), without clearly indicating a superior choice.

Natural convection plays a crucial role in heat and mass transfer within the atmosphere. Despite its fundamental importance, several aspects of this phenomenon remain poorly understood even on a simplified level of controlled RBC conditions and require further investigation. One such example is the scaling of scalar fields, recently discussed by Kumar and Verma (2018). The authors examined the validity of the Taylor frozen hypothesis in the context of thermally driven turbulence in RBC systems, concluding that the hypothesis holds true only when a steady LSC is present in the flow. They also raised doubts about the suitability of the temperature field for determining whether the Bolgiano-Obukhov (BO, $-7/5$) or Obukhov-Corrsin (OC, $-5/3$) scaling applies to turbulent convection. This uncertainty stems from the ambiguous power law behavior of temperature spectra and the challenges in comparing the associated scaling factors. Similar concerns are highlighted in Lohse and Xia (2010), where the authors reviewed structure functions in RBC and suggested that the limited scale separation between the Bolgiano and outer length scales could be the main problem in obtaining BO scaling. In RBC systems, temperature serves as the primary driver of the convective mechanism rather than behaving as a passive scalar, leading to temperature spectra that may deviate from predictions based on passive scalar theories which are often applied in atmospheric analyses. Additionally, He and Xia (2019) demonstrated that a single RBC system can exhibit distinct local dynamics due to the coexistence of different types of force balances. Consequently, applying a single physical mechanism to describe the entire convection cell may oversimplify its complex dynamics.

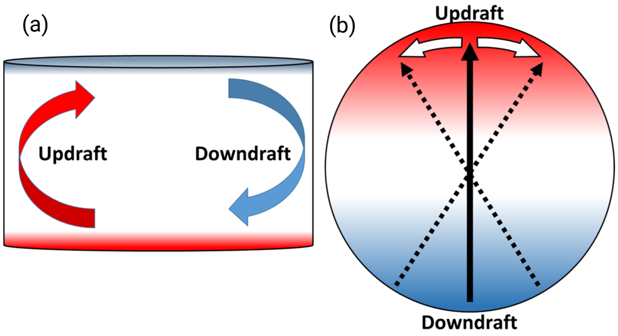

Figure 2. Schematic of the Π Chamber **(a)** and its plan view **(b)** with the marked LSC. **(a)** The arrows represent the mean direction of the warm updraft (red) and the cool downdraft (blue). **(b)**. The dotted and white arrows show the azimuthal oscillations in the circulation. Figure from Anderson et al. (2021).

From a microphysical perspective, which is the primary application of the chamber, understanding the spatial variability of scalar fluctuations within the chamber, including the properties of the LSC, is crucial. This understanding impacts not only the positioning of instruments inside the chamber but also the strategies for measurements, such as the lengths of measurement time series. Only with insight into the physics involved can different phenomena be effectively linked together. This is why analyses aimed at addressing the full spectrum of scales are the focus of the present study.

2 Methods

2.1 Setup and experimental strategy

In our measurements, we utilized the most recent version of the UFT, namely UFT-2B, as outlined in Section 1. The schematic representation of the complete UFT setup can be observed in Fig. 3. The sensor head was affixed to a $1\ \mathrm{m}$ probe support and linked to a specially designed $1\ \mathrm{mA}$ bridge/amplifier (AMP) using an approximately $1\ \mathrm{m}$ standard BNC cable. This amplifier was powered by four AA batteries. Subsequently, the analog signal was acquired by a 16-bit resolution digital-to-analog converter (DAC) from Measurement Computing Corporation (MCC). The DAC had a sampling rate of up to $100\ \mathrm{kS\,s^{-1}}$ (S stands for samples) and utilized the dedicated MCC software DAQami. Despite the time constant allowing for about $10\ \mathrm{kHz}$ data collection, we opted for an oversampling rate of $20\ \mathrm{kHz}$ to facilitate post-processing and filter out artifacts from other lab systems. Using two head sensors during this study, each possessing an approximate resistance of 30 Ω, we attained a UFT sensitivity of approximately $75\ \mathrm{mV\,K^{-1}}$ after calibrating with a standard thermocouple.

For vertical profiling, the UFT was attached to a $6\ \mathrm{mm}$ diameter, $1.5\ \mathrm{m}$ long rod with a 90 degree bend at the end. The rod was marked in $3\ \mathrm{cm}$ increments to facilitate easy UFT positioning. A sturdy metal stand with two adjustable clamps was used to secure the rod in a stable, vertical position while allowing for the user to manually move the UFT to the desired location (see Fig. 3). To minimize potential movements of the UFT cabling and sensor head, both were affixed to the rod using simple adhesive, maintaining the wire in an upward and parallel orientation to the floor.

We studied the small-scale temperature structure within the convection environment across three temperature differences between the chamber's floor and ceiling: $10\ \mathrm{K}$, $15\ \mathrm{K}$, and $20\ \mathrm{K}$, as detailed in Table 1. The measurement setup included the cylindrical thermal panel ($1\ \mathrm{m}$ high, $2\ \mathrm{m}$ diameter), which is not shown in Fig. 3. For a more detailed schematic, please refer to Chang et al. (2016).The Rayleigh number was on the order of $\sim 10^9$ for the set boundary conditions and the chamber height of 1 m. We performed our calculations based on the formula suggested by Niedermeier et al. (2018), assuming dry convection with an estimated Prandtl number of 0.72.

Our primary focus was on examining scalar fluctuations throughout the entire vertical dimension, with a particular emphasis on regions near the floor and the ceiling. To achieve this, the UFT deployments featured irregular measurement positions (see Table 1) increasing slightly the spatial resolution of measurements near the both plates. Another consideration was the variable measurement time t, ranging from $3\ \mathrm{min}$ to $19\ \mathrm{min}$. Such choice was dictated by the chamber's operational schedule, which constrained both the number of sampled points and the range of explored conditions.To quantify whether the measurements are converged, we employed the framework provided by Lenschow et al. (1994). According to the results presented by the authors, when the ratio of the measurement time t to the large eddy correlation time t_c ratio gives $t/t_c \approx 10$, the data is within approximately 10% of the *true* value. Considering the turbulent properties, we link t_c with the large eddy correlation time for the turbulence flow, which is estimated to be on the order of several seconds, $10\ \mathrm{s}$ in calculations, assuming a mean flow velocity of tens of centimeters per second. In this case, the averaging time of $3\ \mathrm{min}$ corresponds to approximately $18t_c$, whereas for $19\ \mathrm{min}$ time series it gives $114t_c$ indicating satisfactory convergence for atmospheric applications.

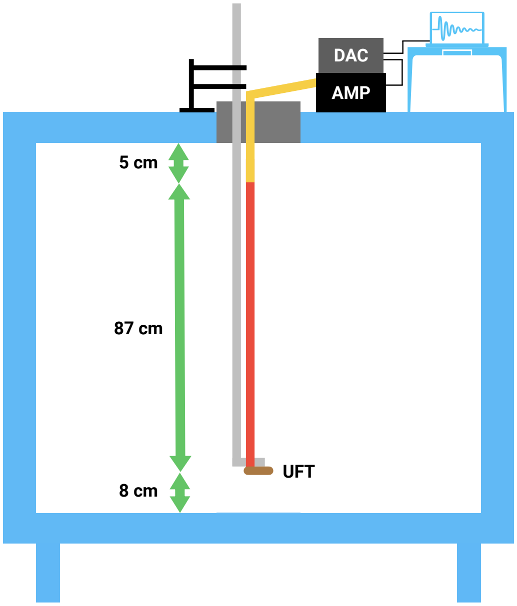

Figure 3. Schematic of the setup used during the measurements (diagram not to scale). At the top there was an operations center housing with most of the devices and cabling, including a BNC cable (yellow), an UFT amplifier (AMP), digital-to-analog converter (DAC), and a PC with a DAC software. Inside the Π Chamber, a vertical rod with a curved end (gray) and a UFT sensor (brown) with DANTEC® probe support (red) attached to that end was deployed. The profiling limits were about 8 cm above the bottom and around 5 cm below the top layer. Note that, for clarity, the schematic does not include the cylindrical thermal panel which was installed during the measurements.

A less emphasized aspect was the surface topography. One configuration involved the presence of rough boundaries, consisting of aluminum bars (4 cm wide and 1.4 cm high) positioned on the floor and ceiling forming longitudinal stripes separated by 17 cm intervals. The bars themselves were at a slightly different temperature compared to the rest of both panels (approximately 0.4 K). Subsequent UFT deployments were conducted after removing the bars, aiming to compare temperature fluctuation properties between the two cases. Unfortunately, a portion of the dataset is invalid due to high battery drainage, resulting in coverage of only one rough boundary case in this study.

As the surfaces inside the chamber reached steady temperatures (refer to Tab. 1), the UFT sensor was initially positioned 8 cm above the floor, near the axis of the cell. Due to the rod's length inside the chamber corresponding to its height, we had to wait for some time to allow the vibrations of the head sensor to dampen. This was really important after each position (h) change but played a crucial role especially in profiling the lower half of the measurement volume. The chamber's flange was covered with a thick foam layer, effectively reducing most mixing events near the opening. Although not an ideal solution, it seemed the most reasonable choice considering the ease of checking the UFT position, as well as the insulating and damping properties of the foam (when coating the rod).

Table 1. List of experiments together with the corresponding Π Chamber and UFT settings, and the Rayleigh numbers. Symbols explanation: T_F, T_C, T_W represent floor, ceiling, and walls temperature respectively, t stands for the measurement time at a given height h above the floor. Names of the experiments are made as follows: type of the measurement ("V" for vertical), ΔT, type of boundaries (*S* for smooth or *R* for rough), and time spent at a single position (*L* for 19 min or no marking for 3 min).

Experiment	rough/smooth boundaries	T_F [$^\circ$C / K]	T_C [$^\circ$C / K]	T_W [$^\circ$C / K]	h [cm]	t [min]	Ra [$\times 10^9$]
V10-S-L	smooth	25 / 298	15 / 288	20 / 293	irregular	19	1.1
V10-S	smooth	25 / 298	15 / 288	20 / 293	8–95	3	1.1
V15-S-L	smooth	27.5 / 300.5	12.5 / 285.5	20 / 293	irregular	19	1.6
V15-S	smooth	27.5 / 300.5	12.5 / 285.5	20 / 293	8–95	3	1.6
V20-S-L	smooth	30 / 303	10 / 283	20 / 293	irregular	19	2.1
V20-S	smooth	30 / 303	10 / 283	20 / 293	8–95	3	2.1
V20-R	rough	30 / 303	10 / 283	20 / 293	8–95	3	2.1

The irregular positions are: 8, 14, 26, 35, 50, 65, 74, 86, 95 [cm].

After completing the measurements, the dataset underwent several basic preparations. These included the removal of electronic artifacts, signal despiking, Butterworth filtering (10th order, 2 kHz cuttoff frequency), 2 kHz averaging, and the translation of values from voltage to temperature units. Additionally, each time series was consequently normalized by subtracting mean temperature value in the given position (see e.g., Fig. 4).

2.2 DNS methodology

Cloud Model 1 (CM1) (Bryan and Fritsch, 2002) in DNS configuration is used for these simulations. The model and setup are described in detail in Chandrakar et al. (2022, 2023). The computational domain size for DNS is 960 $\times$ 960 $\times$ 500 grid cells with a homogeneously 2.083 mm grid spacing in horizontal and stretched grid in vertical (finer near the top and bottom boundaries). Note the computation domain represents a rectangular parallelepiped system rather than a cylindrical setup used during the experiments. CM1 solves the conservation equation set with the Boussinesq approximation and a prognostic pressure equation using a three-step Runge–Kutta time integration method with a fifth-order advection scheme. The Klemp-Wilhelmson time-split steps are used for the acoustic terms in the compressible solver. The time integration of the governing equations uses an adaptive time step with a maximum Courant–Friedrichs–Lewy (CFL) number of 0.8. A no-slip boundary condition for all walls is applied, and the temperature boundary conditions (constant temperatures) are the same as the experimental setup. The simulations use molecular viscosity and thermal diffusivity values at the mean temperature (Prandtl number = 0.72). DNS is performed for the three experimental cases, V20-S, V15-S, and V10-S, listed in Tab. 1. Outputs from a steady-state period after the initial spin-up are used for the analysis. Consistent with the experiments, the Eulerian temperature time series are outputted at 0.0012–0.0015 s intervals from a region near the center of the domain (95–105 cm from sidewalls) at multiple heights from the bottom surface.

3 Results

3.1 Determination of basic characteristics of temperature profile

The top panel of Fig. 4 provides a sample of temperature fluctuations T' ($T' = T_h - \overline{T}_h$, where T_h represents the temperature series at a given height h, and overline denotes the mean) from the vertical scan of the measurement volume near the axis of the chamber. The skewed fluctuations observed in the closest proximity to the plates serve as expected temperature evidence of thermal plumes characteristic for RBC. We can observe a smooth transition involving gradual suppression of fluctuations or rather gradual decrease in occurring thermal plumes as the sensor moved towards the mid-height plane. The reverse symmetry is present in the upper half of the cell. The nature of these fluctuations aligns with the numerical results of heat fluxes in the bulk region obtained by Lakkaraju et al. (2012), temperature time series reported in He and Xia (2019) and Wang et al. (2022), and experimental data provided by Anderson et al. (2021). However, it is noteworthy that all these works primarily focused on specific regions of the cells, lacking a more detailed insight into the temperature characteristics, especially considering the limited temporal resolution of the used instrumentation.

The most substantial temperature fluctuations are observed near the floor region. In cases with a flat surface (experiments summary in Tab. 1), peaks oscillate around 4 K, while rough boundaries scan exhibit fluctuations exceeding 5 K. As the sensor approaches the mid-high plane, the differences between $\Delta T = 20$ K cases become negligible. Similarly, no distinctions are apparent near the upper plate, with a maximal amplitude at the level of -4 K for both V20-S and V20-R.

In the bottom panel of Fig. 4, two vertical layouts are presented, each illustrating 10 min series near both plates positions and segregating T' based on the given ΔT. The evident reverse symmetry is notable; however, it is important to highlight that there are varying amplitudes of fluctuations in each corresponding pair of graphs (same ΔT but distinct h). This variation may result from weaker thermal plumes departing from the top plate, as well as from the not perfectly insulated chamber's flange (mentioned in 2.1), which could lead to minor mixing in the vicinity of the sensor deployment spot. For a more in-depth examination of the temperature fluctuations near both plates, refer to Appendix A.

The temperature fluctuations also manifest oscillations, particularly noticeable in the case of $\Delta T = 20$ K near the plates. However, these oscillations gradually diminish as the temperature difference decreases and as the sensor moves toward the center of the cell. Analyzing V20-S-L at both heights, the periodicity appears irregular but is of a same order of magnitude as observed by Anderson et al. (2021) and therefore corresponds to the LSC. Previous studies have highlighted that the LSC can exhibit various modes around its mean position, leading to phenomena such as out-of-phase oscillations at the top and bottom of the chamber (torsional mode, see Funfschilling et al. (2008)), as well as side-to-side oscillations (sloshing mode, see Xi et al. (2009); Brown and Ahlers (2009)). Cells with very high symmetry might be also characterized by spontaneously cease and reorientation of the LSC to different angular position (Brown and Ahlers, 2009). All these effects are beyond the scope of this investigation but the raw measurements give clear evidence of temperature oscillations near both plates.

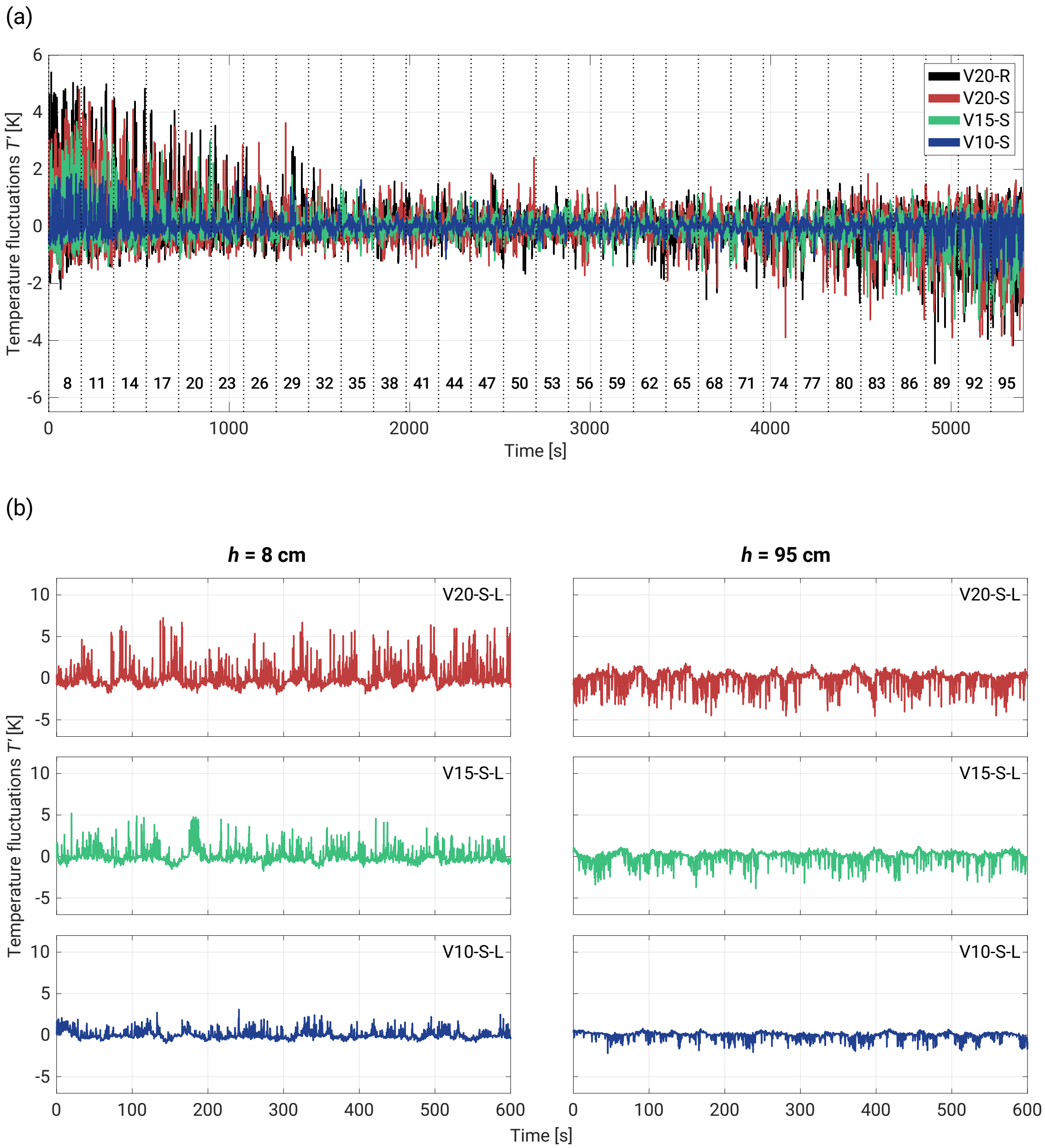

Figure 4. Temperature fluctuations T' time series corresponding to different ΔT that are described in Tab. 1. Top panel **(a)** shows time series collected during full vertical scans with the consecutive changes of the sensor positions across the chamber. The horizontal row of numbers denote the heights in centimeters above the lower plate. The chart includes 3 min series. Lower panels **(b)** represents 10 min measurements near the floor ($h = 8$ cm), and just below the ceiling ($h = 95$ cm, 5 cm below the top plate).

In Fig. 5, the standard deviation $\sigma_{T'}$ is presented in relation to the sensor position within the chamber and illustrates the dependence of the fluctuation level, corresponding to the top panel of Fig. 4. The highest $\sigma_{T'}$ values are observed near both plates with the maximum at the bottom. This asymmetry diminishes as ΔT decreases, starting with an approximate 0.4 K disparity in V20-R and concluding with about a 0.1 K shift in V10-S-L. It's noteworthy that extended measurements yield slightly different values, reflecting a more robust convergence as opposed to 3 min cases. The bulk region exhibits relatively constant values with comparatively small deviations. Additionally, this region experiences the smallest differences between corresponding ΔT values. Decreasing ΔT shifts left $\sigma_{T'}$ values and damps T' in the whole volume. In Fig. B1a we provide non-dimensionalized form of standard deviation.

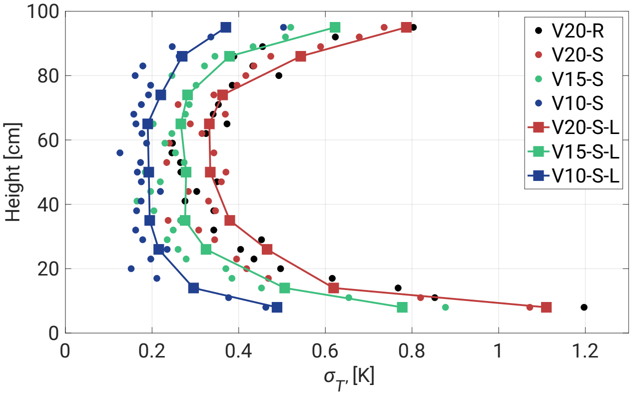

Figure 5. Standard deviation $\sigma_{T'}$ with respect to the position of the sensor. Short time series (3 min) are denoted by circles, squares represent longer measurements (19 min). Decreasing ΔT shifts left $\sigma_{T'}$ values reducing the temperature fluctuations at all positions.

The surface topography contributes to slightly higher $\sigma_{T'}$ values, primarily in the closest vicinity of the plates. This effect may be attributed to the elevated surface level, potentially leading to varied stages of thermal plume development at the same measurement position. However, these thermal structures are getting mixed with the surroundings, producing approximately equivalent results just a few centimeters higher. As previously mentioned, He and Xia (2019) emphasized that each region of the RBC can exhibit its local dynamics, a consequence of overlapping mechanisms that act as drivers for each other. In this specific case, the LSC induces mixing of all thermal structures originating from the surface. It can also turbulently propel thermal plumes due to irregular topography. The resulting mixing and stronger turbulence in this region might be responsible for the thermal peaks observed in the top panel of Fig. 4.

In Fig. 6, the skewness of T', denoted as $\gamma_{T'}$, is analyzed with respect to the vertical positions within the chamber. We use adjusted Fisher–Pearson standardized third moment, expressed as $\gamma_{T'} = \frac{N^2}{(N-1)(N-2)} \frac{\overline{T'^3}}{\sigma_{T'}^3}$, where N represents the number of samples. The findings confirm previous observations, showing positive skewness (associated with warm plumes) near the floor and negative skewness (indicative of cold plumes) just below the ceiling. The third moment is notably influenced by rare events, leading to significant fluctuations in the 3 min dataset but mostly averaged out in longer segments, resulting in more consistent curves.

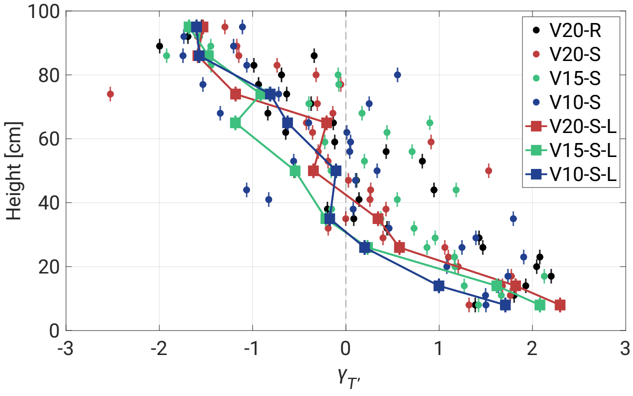

Figure 6. Skewness $\gamma_{T'}$ with respect to the position of the sensor. Short time series (3 min) are denoted by circles, squares represent longer measurements (19 min). Uncertainties were calculated using formula $\delta_{\gamma_{T'}} = \sqrt{\frac{6N(N-1)}{(N-2)(N+1)(N+3)}}$ where N denotes the number of samples.

The regions near both plates demonstrate data convergence of $\gamma_{T'}$ values with minimal deviations. An interesting observation is noted at a distance of 8 cm above the floor, where the 3 min records initially exhibit a skewness of about 1.4. This area likely experiences a higher frequency of intense thermal plumes, resulting in a broader range of temperature fluctuations (refer to Fig. 5). It has been shown in previous studies that thermal plume detachment introduces large fluctuations in temperature and velocity boundary layer thickness (Wagner et al., 2012; Shi et al., 2012; De et al., 2018; Shevkar et al., 2022). Similar effects might be responsible for what we observe. As the plume structures develop, $\gamma_{T'}$ increases to approximately 2. Then, at the 20 cm level, there is a subtle indication of possible change in the thermal dynamics of the system. This change may be associated with specific transitions in convective flow patterns and more intense interaction of thermal plumes with the LSC in the ring layer around the walls and plates (see Fig. 2a). Moving further away from the heated floor, the LSC is likely dominating the existing structures, increasing the dissipation of thermal energy and leading to a decrease in skewness. This results in thermal structures becoming more dispersed, leading to a narrower and less extreme distribution of temperature fluctuations.

However, not all thermal plumes could be fully averaged out, especially as the flow around the cell decreases towards more central regions. This might allow some remaining plume structures to reach the central region between 40–70 cm and mix which could result in positive skewness (bottom plumes carry higher energy). Similar behavior might be also observed in longer records, manifesting as fluctuations in $\gamma_{T'}$ within the 50–70 cm segment. Importantly, the positions of these shifts do not appear to be directly dependent on ΔT.

A comprehensive understanding of the thermal dynamics requires additional information on the small-scale temperature field around the axis, its velocity field, and a detailed description of the LSC time evolution. From the perspective of microphysical processes in future moist experiments, the Lagrangian histories of droplets or aerosols carried by thermal plumes–or alternatively located in the volumes between them–can theoretically lead to different droplet sizes (Chandrakar et al., 2018b, 2023).

The local variability of $\sigma_{T'}$ and $\gamma_{T'}$ indicates that, over short timescales, droplets present in a given volume of the chamber may develop differing growth habits.

Upon comparing the topographic effect, we did not observe any major differences and concluded that 3 min records might be insufficient to investigate the impact caused by the presence of roughness. However, recent numerical work by Zhang et al. (2018) (for $10^7 \leqslant \mathrm{Ra} \leqslant 10^{11}$ and fixed $\mathrm{Pr} = 0.7$) indicates that there is a critical roughness height h_c below which the presence of roughness reduces heat transfer in RBC. The authors link this phenomenon with fluid being trapped and accumulated inside the cavity regions between the rough boundaries. Our approximate calculations for the Π Chamber setup indicate the h_c of approximately 7 mm, compared to the 1.4 cm height of the tiles.

3.2 Power Spectral Densities

Power Spectral Density (PSD) of T' was computed using the Welch algorithm. Initial analyses were primarily directed towards estimating the LSC periods τ for the given ΔT and with respect to the measurement position (see Fig. 7a). This involved utilizing 19 min datasets with window lengths approximately equal to the size of the collected segments. Employing a 50% overlap between segments and incorporating a high number of discrete Fourier transforms (eight times the window length), we derived estimates of the LSC periods along with their associated standard deviations. For $\Delta T = 10$ K a modest convergence of data points is observed, particularly notable within the 60–80 cm region. This resulted in relatively elevated standard deviation (grey areas denote +/- $1\sigma_\tau$), yielding a period of approximately $\tau_{10} \approx 79$ s. Subsequent ΔT demonstrated a more uniform distribution across all levels, accompanied by a gradual reduction in the LSC period to approximately $\tau_{15} \approx 65$ s and $\tau_{20} \approx 57$ s.

The relationship between τ and ΔT, modeled by the power law function τ^{e}, is illustrated in Fig. 7b. The fit exhibits narrow 95% prediction bounds in the fitted region but significantly large bounds outside. The model was constructed using a sparse dataset consisting of only four data points, including the result obtained by Anderson et al. (2021) at $\Delta T = 12$ K. Consequently, this limited dataset may not fully capture the true relationship, particularly at lower ($\Delta T < 10$ K) and higher ($\Delta T > 20$ K) temperature differences. The potential discrepancies could be attributed to a stronger diffusion dominance over convection at lower ΔT or more pronounced overlapping thermal plumes at higher temperatures, respectively.

In subsequent PSD analyses, we continued using only 19 min records, as shorter measurements exhibit too much variability in spectra due to their duration being comparable with the LSC periods. This time-modified window length, approximately 1/9 of the total segment with windows overlapping by half of their length, resulted in 17 individual PSDs that were averaged. This approach enhances chart readability while maintaining fidelity to the spectral slopes. To collapse the curves representing measurements from different positions, we followed the scaling method proposed by Zhou and Xia (2001). Fig. 8a plots the scaled $f^2P(f)$ spectrum for the V20-S-L case, enabling determination of the peak frequency f_p, around which the PSDs become universal functions. In this case, f_p oscillates around $f = 4$ Hz, exhibiting high convergence across all curves.

In Fig. 8b, we provide a sample of scaled PSD $P(f)/P(f_\mathrm{p})$ versus f/f_p in the lower half of the chamber and define three spectrum regimes. Based on the scaling method proposed by Kumar and Verma (2018) and Zhou and Xia (2001), we conducted also a similar analysis in the wavenumber domain. For more details, please refer to Appendix C. To estimate the slopes, we employed a methodology outlined in Siebert et al. (2006) and Nowak et al. (2021), averaging raw spectra over

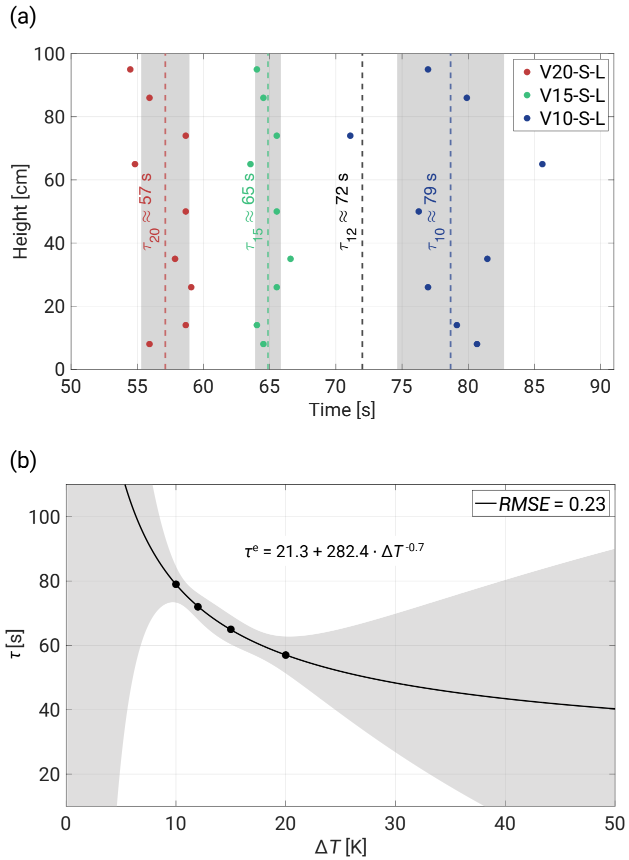

Figure 7. Measured LSC periods with respect to ΔT and vertical position of the sensor. **(a)** Grey regions describe +/- $1\sigma_\tau$ and the black dashed line denotes the result obtained by Anderson et al. (2021) for $\Delta T = 12$ K. **(b)** The relationship between τ and ΔT modeled by the power law (τ^{e}) function. The plot includes 95% simultaneous functional bounds, fitted equation, and root mean squared error ($RMSE$).

equidistant logarithmic frequency bins (twenty bins per decade in our case) and then fitting power law functions. To obtain the best possibly fit we selected spectra regions based on the highest log-log linearity criteria using the Pearson correlation coefficient p for the resampled points.

Extended discussions on passive scalar spectra scaling can be found in works such as Gotoh and Yeung (2012) and Sreenivasan (2019). We adapted the graph from the former study for Fig. 9, which illustrates possible spectral slopes as a function of the Pr number. For our experimental conditions, the results are expected to align with the scaling for Pr ≈ 1. In the following paragraphs, we aim to contextualize our findings within the broader scope of the literature and address potential explanations for observations that have not yet been described.

In Fig. 10a, the regime $0.2 \leqslant f/f_{\mathrm{p}} \leqslant 1$, marked by circles, in the literature is referred to as the inertial-convective regime which is associated with OC scaling, where the temperature field (acting as a passive scalar) does not influence the flow dynamics (Castaing, 1990; Cioni et al., 1995; He et al., 2014). However, in thermally-driven convection, the flow is actively

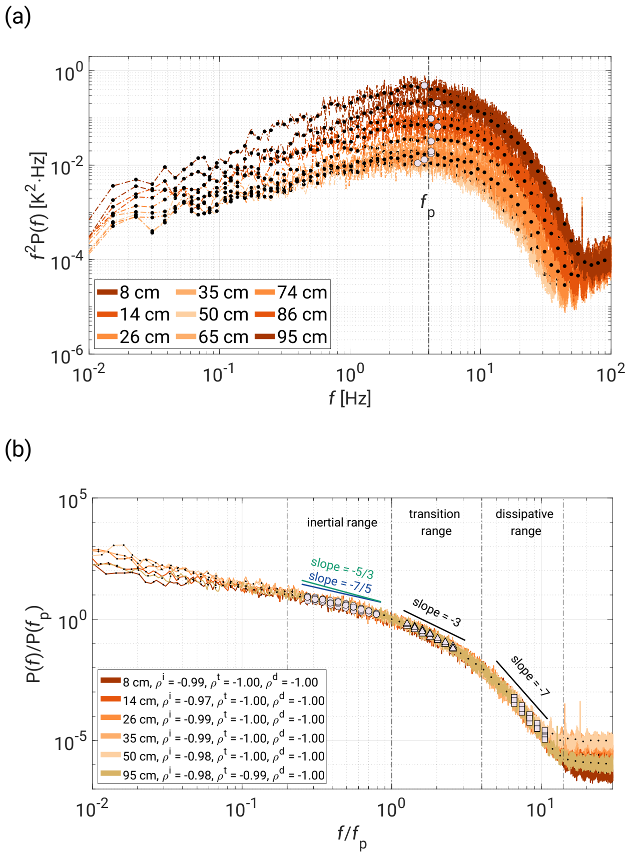

Figure 8. Scaled V20-S-L PSD with respect to the UFT positions (color gradients) in the chamber. **(a)** Scaled spectrum of $f^2P(f)$ across the chamber volume and with marked mean f_p value, $f_\mathrm{p} \approx 4$ Hz. **(b)** PSD $P(f)/P(f_\mathrm{p})$ versus $f/(f_\mathrm{p})$ with three defined regimes: inertial range (circles, $0.2 \leqslant f/f_\mathrm{p} \leqslant 1$), transition range (triangles, $1 \leqslant f/f_\mathrm{p} \leqslant 4$), and dissipative range (squares, $4 \leqslant f/f_\mathrm{p} \leqslant 20$). Each regime is denoted by different markers with an approximate slope value added above curves. The Pearson correlation coefficients p have upper indices to indicate the regimes. Please note that the results presented in the bottom panel cover positions from the lower half of the chamber as well as the top position.

driven by temperature-induced buoyancy differences. This range is therefore redefined as the inertial-buoyancy range, where the temperature spectrum follows BO scaling (Chillá et al., 1993; Ashkenazi and Steinberg, 1999; Zhou and Xia, 2001). Our analysis provides no definitive answer, as the slopes oscillate between OC and BO scaling, with a slight bias toward $-7/5$. However, as previously noted, the two slopes are too close to be easily distinguished (see Fig. 8b). Thus, we classify this range simply as the inertial range without committing to a specific scaling profile. Interestingly, Niemela et al. (2000) ($10^6 \leqslant \mathrm{Ra} \leqslant 10^7$) and Pawar and Arakeri (2016) (axially homogeneous buoyancy-driven turbulent flow, $10^4 \leqslant \mathrm{Ra} \leqslant 10^9$) observed both scaling behaviors in their experiments. The latter study raised the question of whether these results indicate dual scaling or a gradual steepening of the spectrum.

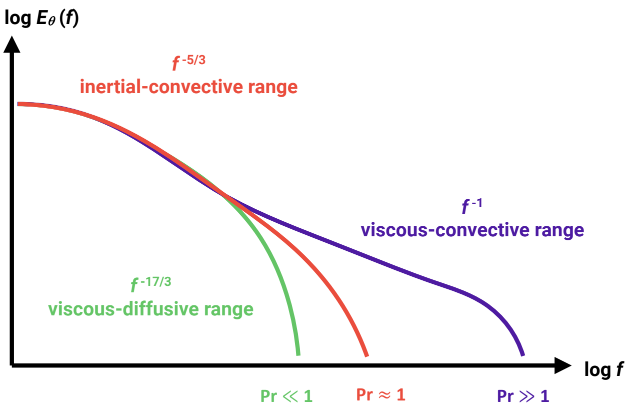

Figure 9. Schematic of passive scalar spectrum depending of Pr regime. Figure based on the graph from Gotoh and Yeung (2012) with minor modifications.

No direct references in the literature address the subsequent regime scalings (~ -3 and ~ -7) or the roll-off region of the scalar spectrum (see Fig. 9). Recent investigations of the dissipation range in the energy spectrum only began exploring this regime suggesting a superposition of two exponential forms (Khurshid et al., 2018; Buaria and Sreenivasan, 2020). Therefore, our further discussion will explore potential connections between our and other results in convective flow research.

The -3 scaling might simply represent a crossover into the following dissipative range but the mid-range scales in the system could also be subjected to more subtle phenomena. RBC dynamics span a wide range of scales, including thermal plumes, vortices, and the LSC, with complex interactions between these structures (Fernando and Smith IV, 2001; Xi et al., 2004; Zhou et al., 2016; Guo et al., 2017; Chen et al., 2018; Pandey et al., 2018; De et al., 2018; Dabbagh et al., 2020; Wang et al., 2022; Yano, 2023; Yano and Morrison, 2024). These overlapping processes likely influence the observed spectra. Recent LES studies on thermal plumes have revealed additional insights into scalar spectral scaling (Chen and Bhaganagar, 2021, 2023, 2024). Using a heated surface experiment, the authors reported density and temperature spectra scaling as -2.7, strongly correlated with the velocity spectrum. Furthermore, vertical heat and mass fluxes exhibited a -3 scaling, matching the vertical component of the turbulent kinetic energy (TKE) spectrum. This corresponds with the regime $1 \leqslant f/f_\mathrm{p} \leqslant 4$ marked by triangles in Fig. 10a, which is characterized by slopes oscillating around -3, with slightly greater variability observed for the V10-S-L case.

Moreover, in the papers by Chen and Bhaganagar both spectra of 2D TKE, horizontal structures of 3D TKE, as well as helicity, consistently exhibited slopes of $-5/3$ and -3 respectively. Their flux analysis revealed inverse TKE and helicity cascades toward large structures and forward cascades of these invariants for the small scales. Further studies on velocity-based longitudinal structure functions (2nd, 3rd, and 4th moments) showed that the scaling exponents fell between theoretical predictions for 2D and 3D systems. For example, strong vertical confinement or anisotropic Fourier mode distributions can mimic 2D dynamics in certain ranges (Musacchio and Boffetta, 2019; de Wit et al., 2022; Alexakis, 2023). Consequently, energy cascades and their directions are highly scale-dependent, influenced by invariants such as enstrophy and helicity, potentially resulting in the coexistence of multiple cascades and the superposition of power law spectra. Detailed discussions on cascades and transitions in turbulence are provided by Alexakis and Biferale (2018). However, in the Π Chamber we do not recognize strong anisotropy and only regions near the top and bottom plates could potentially exhibit such quasi 2D, effects whereas similar spectra slopes are observed in the whole volume of the chamber. On the other hand, in 3D turbulence, large-scale stirring can introduce helicity, modifying cascade directions and contributing sub-leading corrections depending on the helicity's sign (Eidelman et al., 2014; Yan et al., 2020; Plunian et al., 2020). The exact role of helicity in energy transfer mechanisms remains unclear and is an active area of research (Yao and Hussain, 2022).

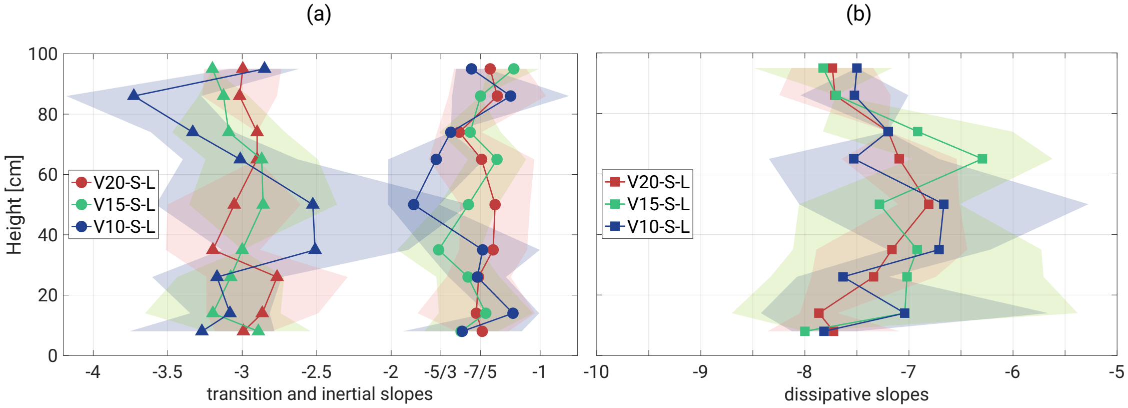

Figure 10. Panel of fitted slopes. **(a)** corresponds to transition and inertial ranges respectively whereas **(b)** describes dissipative regime. The slopes are accompanied by 95% confidence bounds except in a few cases where the slopes were manually fixed due to fitting difficulties.

Given this complexity, it is reasonable to question whether theoretical assumptions such as isotropy, homogeneity, stationarity, and self-similarity are sufficient to capture the full physical reality. Anisotropy and non-stationary coherent structures likely play significant roles, potentially causing deviations from predicted spectral scaling. In the RBC, temperature forcing drives both large- and small-scale structures, complicating the universality of passive and active scalar theories. Alexakis and Biferale (2018) emphasize that strong assumptions about cascades and their directions are not feasible for active scalars, particularly when velocity and scalar fields are strongly coupled. This leaves open questions about preferential sampling effects of forcing along Lagrangian trajectories of the active scalar field. In the given full spectrum analysis, the nature of the spectral break observed near $f/f_\mathrm{p} \approx 1$ may be linked to a transition between LSC-dominated scales, characterized by large coherent structures, and smaller-scale thermal plumes and vortices. These overlapping power laws could ultimately shape the observed spectra. Consequently, we interpret the -3 regime as a transition range between buoyancy-scale processes and molecular dissipative scales. Additional analysis presented in Appendix D estimates the dominance of thermal plumes near the chamber center. Following He and Xia (2019), we demonstrate a logarithmic dependence of $\sigma_{T'}$ on chamber height, reflecting a balance between buoyancy and inertial forces.

Finally, our high-frequency measurements indicate that the dissipative regime slopes are approximately -7 (see Fig. 10b). The slope distribution with respect to chamber height is symmetrical, reaching the steepest values near the plates (~ -8)

and the smallest in the bulk region (~ -7). According to Sreenivasan (2019), no scalar spectrum description exists for the dissipative regime. While the energy spectrum in this range can be represented by an exponential form, our findings suggest that for the scalar field, even a single power law is sufficient. Corresponding characteristics are visible in Niemela et al. (2000) and Zhou and Xia (2001), although these studies provide limited discussion on the observed slopes.

Worth noting is also the variability of the noise level (starting around $f/f_\mathrm{p} \approx 12$) with respect to the chamber height, with its highest values linked to the bulk region and the lowest (10 times magnitude difference) representing regions near the plates (see Fig. C1 in Appendix C). This phenomenon is attributed to the mean velocity field and its strong reduction in the central areas of the cell causing the noise to rise.

3.3 DNS versus experimental data

Another goal of the presented study was to compare the experimental results obtained with the UFT and the corresponding DNS data. The essential details on the DNS methodology and properties of the series can be found in Sec. 2.2. Our approach was to repeat the analysis and to retrieve both basic characteristics of temperature profile and information on PSD at different cell's levels. Sample series can be seen in Fig. A1 and Fig. A2.

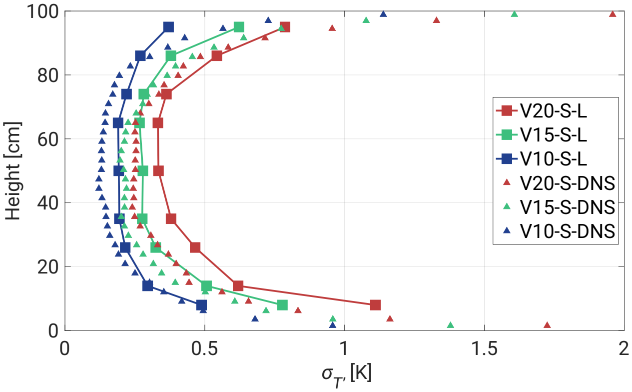

Figure 11. Standard deviation $\sigma_{T'}$ with respect to the height of the chamber. The chart analogical to Fig. 5 but including only $19\,\mathrm{min}$ segments (squares) and the DNS (triangles).

Fig. 11 present analogous to Fig. 5 study but with the DNS data covering exactly same thermodynamic conditions in the cell. Since the vertical grid size spans from about $1\,\mathrm{mm}$ near the plates to about $2.3\,\mathrm{mm}$ at the center, the available range significantly improves comprehensiveness of boundary layers. The limit regions exhibit maximum deviation of $\sigma_{T'} \approx 2\,\mathrm{K}$ with a bias in the vicinity of the upper plate. Also the shape of the curves is more bumped up in the center and slightly shifted left what might be an analogy to $3\,\mathrm{min}$ records in the Fig. 5. The numerical data provide more stable monotonicity but represents equivalent periods of time. In Fig. B1b there is non-dimensionalized form of this figure.

Similar conclusions can be made in terms of skewness profiles in Fig 12a. The DNS data exhibits much smaller fluctuations than corresponding $3\,\mathrm{min}$ UFT segments but preserve the general tendency near the floor and in the central region. The

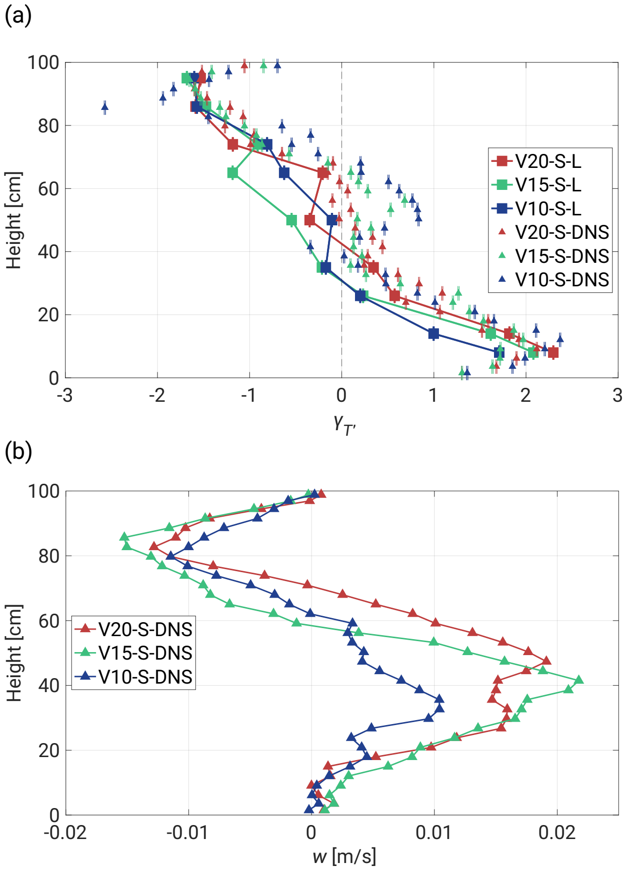

Figure 12. (a) Skewness, $\gamma_{T'}$, as a function of height within the chamber supported by the 3 min DNS data. The chart analogical to Fig. 6 but including only 19 min segments (squares) and the numerical time series (triangles). **(b)** Mean vertical flow profile provided by the DNS.

characteristic jump in $\gamma_{T'}$ is observed not around 20 cm but in half way. On the other side, a symmetrical jump is also observed near the ceiling what was not revealed in the UFT measurements likely due to a very shallow layer of thermal plume regime (the UFT measurements ended about 5 cm below the ceiling). Also the mixing region between 40–70 cm is reestablished resulting in higher deviations for lower ΔT. The skewness distribution contributes to the mean vertical profile in the cell (see Fig. 12b). The presence of both positive ($\sim$40 cm) and negative ($\sim$80 cm) velocity jumps drives dynamics in the bulk region, facilitating the mixing of cold and warm plumes. The horizontal components of the flow follow the LSC directions giving mean values of 15 $\mathrm{cm/s}$ near the plates. A more comprehensive discussion on the dynamics of the thermal plumes can be found in Sec. 3.1. Note that the plots in Fig. 11 and 12 represent single-column data (not the horizontal average), meaning perfect symmetry is not expected, in particular for the period of the LSC circulation.

4 Summary

We conducted a small-scale study on the temperature structure of RBC in the Π Chamber using three temperature differences ($10\ \mathrm{K}$, $15\ \mathrm{K}$, and $20\ \mathrm{K}$) at Ra of approximately 10^9 and Pr of 0.7. The objective was to improve our understanding of thermally-driven convection by analyzing small-scale variations along the chamber's axis. Measurements were performed using a miniaturized UltraFast Thermometer operating at 2 kHz, enabling undisturbed vertical temperature profiling from 8 cm above the floor to 5 cm below the ceiling. Unlike classical RBC studies, this research is characterized by relatively short measurement durations of 19 min and 3 min, which fall below the typical record lengths for such experiments. Nevertheless, the primary goal was to link this work with other experiments conducted in the Π Chamber. Its main objective is to investigate microphysical processes relevant to the real atmosphere, such as supersaturation fluctuations crucial for cloud formation and development. Small-scale temperature profiling under varying conditions, as typically observed in the chamber, provides valuable insights that could inform future experiments and address related scientific questions. The key findings of this study are summarized below.

- **Basic Characteristics**: We observed significant changes in the standard deviation and skewness of the distribution of temperature fluctuations near the top and bottom surfaces. Additionally, we see variations in the spectra scaling in these near-surface regions. The turbulence in the center of the chamber exhibited characteristics more akin to homogeneous, isotropic turbulence. These observed variations were attributed to the dynamics of local thermal plumes and their interaction with the large-scale circulation (LSC). Both 19 min and 3 min measurements were consistent, although the shorter records showed higher variability in standard deviation and skewness distribution. The statistical properties of the temperature field obtained in the Π Chamber may offer insights into thermal structures development in the atmospheric surface layer, thereby enhancing our understanding of surface-air temperature fluctuations characteristics with respect to the thermal conditions (Kukharets and Nalbandyan, 2006). Furthermore, the analysis of large-scale coherent structures in RBC provides a framework for broader perspective on thermal circulations, as well as the distribution of temperature and moisture, both in cloud chambers (Anderson et al., 2021) and by analogy in the lower atmosphere (Zhou and Xia, 2013; Moller et al., 2021). The chamber is not designed for idealized RBC experiments. Its structure solutions (e.g. windows on sides, atypical side-wall boundary conditions) aimed at cloud microphysics research is revealed in asymmetries of the profiles of temperature fluctuations statistics.

- **Topographic Effects**: No major differences were observed corresponding to topographic effects, likely due to insufficient time series. However, numerical work by Zhang et al. (2018) shed light on the necessary roughness height for robust heat transfer in RBC. Below the critical point, the authors observed trapped and accumulated heat inside the cavity regions between the rough boundaries.

- **Dynamic Regimes**: PSD analysis revealed periodicity of LSC with respect to the temperature differences, characterized by the power law formula consistent with previous findings (Anderson et al., 2021). We identified three distinct dynamic regimes: an inertial range (with slopes of $\sim -7/5$), a transition range (slopes of ~ -3), and a dissipative range (slopes of ~ -7). The scale break between the inertial and transition ranges was attributed to a dynamic transition from the LSC-dominated regime to the thermal plume regime. Appendix D demonstrated that this transition is also observable in the spatial domain. Our findings are consistent with other studies not directly related to RBC though. For example, a similar scale break between inertial and transition ranges was observed in temperature fluctuation measurements near the surface of Jezero Crater on Mars (de la Torre Juárez et al., 2023), whereas slopes of $-17/3$ and -3 have been reported in power spectra of solar surface intensity variance field, attributed to buoyancy-driven turbulent dynamics in a strongly thermally diffusive regime (Rieutord et al., 2010).

- **Experiment Versus DNS**: Experimental findings showed convincing agreement with DNS conducted under similar thermodynamic conditions, marking a rare comparative analysis in this field. Velocity profiles supported the argument for the nature of thermal plumes, and a method to convert spectra from the frequency domain to the wavenumber domain was detailed (see Appendix C). Despite the presence of imperfect boundaries such as window flanges, sampling ports, and instrumentation, idealized DNS provided a reasonable representation of the actual Π Chamber flow, indicating that DNS adequately resolves surface layer fluxes. These results are valuable for improving and validating numerical research, such as sub-grid Large-Eddy Simulation models (Salesky et al., 2024), as well as heat transport models (Goluskin, 2015).

Data availability. The measurement records collected within this study are available from the authors upon request.

Appendix A: Quicklooks of temperature fluctuations

The figures illustrate two realizations of temperature fluctuations at the sensor's position under similar conditions (from the experiment and DNS). The presence of filaments or coherent structures, with temperatures close to that of the nearby plate, is clearly visible. It is important to note that this is not a one-to-one comparison of the same flow but rather an illustration of the maximal scalar fluctuations observed in both the simulation and the experiment. Despite differences in time resolution, both curves in each case exhibit similar magnitudes. The subsequent zoomed-in segments further emphasize the variability within these realizations.

Appendix B: Non-dimensional representation of standard deviations

Non-dimensionalized profiles of the standard deviation show stronger convergence in longer records compared to their dimensional representation.

Appendix C: Power Spectral Density in wavenumber space

In the atmospheric community, PSD is typically presented in either the frequency or wavenumber domain, depending on preferences or scientific goals. As demonstrated in Section 3.2, the collapsed spectral curves in the frequency domain exhibit three dynamic regimes that characterize thermal convection in the Π Chamber. However, by following the scaling method proposed by Kumar and Verma (2018) and the generalized approach of Zhou and Xia (2001), one can obtain analogous PSD in the wavenumber domain.

The first step of the scaling procedure involves the following transformations:

$$k \approx \tilde{f} = f(2\pi)/U,$$
$$P(k) \approx P(\tilde{f}) = P(f)U/2\pi.$$

where $P(\tilde{f})$ and $\tilde{f}$ represent the scaled frequency spectrum and scaled frequency, respectively. The DNS data revealed a symmetrical profile of the mean velocity U near the axis (see Fig. C1). It gradually decreases towards the bulk region, reaching about $0.02\ \mathrm{m/s}$, and maintains approximately equal values near both plates. The resulting wavenumber spectral curves are rescaled with U and shifted accordingly. To collapse them, we found the Kolmogorov length scale, defined as $\eta = (2\pi)/k_n$, where k_n is the wavenumber noise level, and performed another scaling to obtain the $P(k\eta)$ spectrum. The last step follows the adopted procedure of Zhou and Xia (2001).

In Fig. C2a, we present the estimation of $k_\mathrm{p}\eta$, what is a direct analogy to f_p in Subsection 3.2, for the V20-S-L case in the scaled $k\eta^2 P(k\eta)$ spectrum. Unlike the corresponding plot in the frequency domain (see Fig. 8a), $k_\mathrm{p}\eta$ does not oscillate around one value. Here, we observe a gradual increase in $k_\mathrm{p}\eta$ values towards the bulk region, with the $k\eta^2 P(k\eta)$ maximum occurring around $k_\mathrm{p}\eta \approx 0.5$. Fig. C2b provides the final result of the frequency to wavenumber scaling. Both the slopes and dynamic ranges are conserved, providing a clear analogy to Fig. 8.

Appendix D: Standard deviation scaling

To verify if and where we can observe thermal plume dominance in the chamber, we followed the methodology outlined by He and Xia (2019). They demonstrated a strong connection between plumes and the logarithmic root mean square temperature profile using a different setup, which consisted of water as a working fluid ($\mathrm{Pr} = 4.34$), a rectangular-shaped container with $\Gamma = 4.2$, and Ra varied from 3.2×10^7 to 2×10^8. For our purposes, we analyzed the standard deviation $\sigma_{T'}$ distribution of both the 19 min, 3 min, and DNS datasets. Fig. D1 presents the results for two regions in the semi-log domain–$\sim$ 15–35 cm near the floor (Fig. D1a) and $\sim$ 65–95 cm near the ceiling (Fig. D1b). In the both regimes we provided the respective Pearson correlation coefficients and fitted the curves for 19 min time series.

Each profile in the lower half of the chamber exhibits significant linearity correlation in the given region, including the 3 min experimental dataset. Only the V10-S case notably differs from the remaining results, dropping down to $p = -0.59$. The corresponding area in the upper half gives similarly high indications of the p values, excluding shorter measurements, providing evidence of weaker thermal plume response. This observation is reasonable considering the previous discussion in Sec. 3.1 on differences between both regions of the cell.

It is worth mentioning that the zones outside the selected profiles are clearly dominated by different types of forces, resulting in very local dynamics in the RBC.

Author contributions. RG, RAS, JCA, WC, and SPM designed the study. RG and JCA adapted the UFT instrument and the Π Chamber facility for the measurements. RG and JCA performed the UFT measurements. KKC performed DNS. RG processed and analysed the collected data with advice from RAS, SPM, and KKC. RG wrote the manuscript with contributions from RAS, SPM and KKC (who wrote Subsection 2.2). All authors critically proofread and revised the manuscript.

RG is truly grateful to Marta Wacławczyk and Jun-Ichi Yano for thought-provoking talks and for providing constructive feedback on our work.

Competing interests. The authors have the following competing interests: Szymon P. Malinowski is a member of the editorial board of Atmospheric Measurement Techniques.

Acknowledgements. This project has received funding from the Excellence Initiative-Research University Programme (IDUB) as part of Action IV.4.1 under grant agreement No. BOB-IDUB-622-913/2023.

J. C. Anderson, W. Cantrell, and R. A. Shaw acknowledge support from the U.S. National Science Foundation through grant No. AGS-2113060.

K. K. Chandrakar's contribution was supported by the NSF National Center for Atmospheric Research, which is a major facility sponsored by the U.S. National Science Foundation under Cooperative Agreement No. 1852977.

References

Ahlers, G., Bodenschatz, E., Hartmann, R., He, X., Lohse, D., Reiter, P., Stevens, R. J. A. M., Verzicco, R., Wedi, M., Weiss, S., Zhang, X., Zwirner, L., and Shishkina, O.: Aspect Ratio Dependence of Heat Transfer in a Cylindrical Rayleigh-Bénard Cell, Phys. Rev. Lett., 128, 084 501, https://doi.org/10.1103/PhysRevLett.128.084501, 2022.

Alexakis, A.: Quasi-two-dimensional turbulence, Reviews of Modern Plasma Physics, 7, 31, https://doi.org/10.1007/s41614-023-00134-3, 2023.

Alexakis, A. and Biferale, L.: Cascades and transitions in turbulent flows, Physics Reports, 767-769, 1–101, https://doi.org/https://doi.org/10.1016/j.physrep.2018.08.001, cascades and transitions in turbulent flows, 2018.

Anderson, J. C., Thomas, S., Prabhakaran, P., Shaw, R. A., and Cantrell, W.: Effects of the large-scale circulation on temperature and water vapor distributions in the Π Chamber, Atmospheric Measurement Techniques, 14, 5473–5485, https://doi.org/10.5194/AMT-14-5473-2021, 2021.

Ashkenazi, S. and Steinberg, V.: Spectra and Statistics of Velocity and Temperature Fluctuations in Turbulent Convection, Phys. Rev. Lett., 83, 4760–4763, https://doi.org/10.1103/PhysRevLett.83.4760, 1999.

Bailon-Cuba, J., Emran, M. S., and Schumacher, J.: Aspect ratio dependence of heat transfer and large-scale flow in turbulent convection, Journal of Fluid Mechanics, 655, 152–173, https://doi.org/10.1017/S0022112010000820, 2010.

Blass, A., Verzicco, R., Lohse, D., Stevens, R. J. A. M., and Krug, D.: Flow organisation in laterally unconfined Rayleigh–Bénard turbulence, Journal of Fluid Mechanics, 906, A26, https://doi.org/10.1017/jfm.2020.797, 2021.

Brown, E. and Ahlers, G.: Large-Scale Circulation Model for Turbulent Rayleigh-Bénard Convection, Phys. Rev. Lett., 98, 134 501, https://doi.org/10.1103/PhysRevLett.98.134501, 2007.

Brown, E. and Ahlers, G.: The origin of oscillations of the large-scale circulation of turbulent Rayleigh–Bénard convection, Journal of Fluid Mechanics, 638, 383–400, https://doi.org/10.1017/S0022112009991224, 2009.

Bryan, G. H. and Fritsch, J. M.: A benchmark simulation for moist nonhydrostatic numerical models, Monthly Weather Review, 130, 2917–2928, 2002.

Buaria, D. and Sreenivasan, K. R.: Dissipation range of the energy spectrum in high Reynolds number turbulence, Phys. Rev. Fluids, 5, 092 601, https://doi.org/10.1103/PhysRevFluids.5.092601, 2020.

Castaing, B.: Scaling of turbulent spectra, Phys. Rev. Lett., 65, 3209–3209, https://doi.org/10.1103/PhysRevLett.65.3209, 1990.

Chandrakar, K. K., Cantrell, W., Kostinski, A. B., and Shaw, R. A.: Dispersion Aerosol Indirect Effect in Turbulent Clouds: Laboratory Measurements of Effective Radius, Geophysical Research Letters, 45, 10,738–10,745, https://doi.org/https://doi.org/10.1029/2018GL079194, 2018a.

Chandrakar, K. K., Cantrell, W., and Shaw, R. A.: Influence of Turbulent Fluctuations on Cloud Droplet Size Dispersion and Aerosol Indirect Effects, Journal of the Atmospheric Sciences, 75, 3191–3209, https://doi.org/10.1175/JAS-D-18-0006.1, 2018b.

Chandrakar, K. K., Saito, I., Yang, F., Cantrell, W., Gotoh, T., and Shaw, R. A.: Droplet size distributions in turbulent clouds: experimental evaluation of theoretical distributions, Quarterly Journal of the Royal Meteorological Society, 146, 483–504, https://doi.org/https://doi.org/10.1002/qj.3692, 2020.

Chandrakar, K. K., Morrison, H., Grabowski, W. W., Bryan, G. H., and Shaw, R. A.: Supersaturation Variability from Scalar Mixing: Evaluation of a New Subgrid-Scale Model Using Direct Numerical Simulations of Turbulent Rayleigh–Bénard Convection, Journal of the Atmospheric Sciences, 79, 1191–1210, https://doi.org/https://doi.org/10.1175/JAS-D-21-0250.1, 2022.

Chandrakar, K. K., Morrison, H., and Shaw, R. A.: Lagrangian and Eulerian Supersaturation Statistics in Turbulent Cloudy Rayleigh–Bénard Convection: Applications for LES Subgrid Modeling, Journal of the Atmospheric Sciences, 80, 2261–2285, https://doi.org/https://doi.org/10.1175/JAS-D-22-0256.1, 2023.

Chang, K., Bench, J., Brege, M., Cantrell, W., Chandrakar, K., Ciochetto, D., Mazzoleni, C., Mazzoleni, L. R., Niedermeier, D., and Shaw, R. A.: A Laboratory Facility to Study Gas–Aerosol–Cloud Interactions in a Turbulent Environment: The Π Chamber, Bulletin of the American Meteorological Society, 97, 2343–2358, https://doi.org/10.1175/BAMS-D-15-00203.1, 2016.

Chen, C. H. and Bhaganagar, K.: New findings in vorticity dynamics of turbulent buoyant plumes, Physics of Fluids, 33, 115 104, https://doi.org/10.1063/5.0065322, 2021.

Chen, C. H. and Bhaganagar, K.: Energetics of buoyancy-generated turbulent flows with active scalar: pure buoyant plume, Journal of Fluid Mechanics, 954, A23, https://doi.org/10.1017/jfm.2022.1011, 2023.

Chen, C. H. and Bhaganagar, K.: Turbulent cascading in Buoyant plumes, Environmental Fluid Mechanics, https://doi.org/10.1007/s10652-023-09963-9, 2024.

Chen, J., Yin, Z.-X., and Zou, H.-Y.: Visualization of thermal structures in turbulent Rayleigh-Bnard convection, in: Proceedings 18th International Symposium on Flow Visualization, ETH Zurich, 2018.

Chillà, F. and Schumacher, J.: New perspectives in turbulent Rayleigh-Bénard convection, The European Physical Journal E, 35, 58, https://doi.org/10.1140/epje/i2012-12058-1, 2012.

Chillá, F., Ciliberto, S., Innocenti, C., and Pampaloni, E.: Boundary layer and scaling properties in turbulent thermal convection, Il Nuovo Cimento D, 15, 1229–1249, https://doi.org/10.1007/BF02451729, 1993.

Cioni, S., Ciliberto, S., and Sommeria, J.: Temperature Structure Functions in Turbulent Convection at Low Prandtl Number, Europhysics Letters, 32, 413, https://doi.org/10.1209/0295-5075/32/5/006, 1995.

Dabbagh, F., Trias, F. X., Gorobets, A., and Oliva, A.: Flow topology dynamics in a three-dimensional phase space for turbulent Rayleigh-Bénard convection, Phys. Rev. Fluids, 5, 024 603, https://doi.org/10.1103/PhysRevFluids.5.024603, 2020.

De, A. K., Eswaran, V., and Mishra, P. K.: Dynamics of plumes in turbulent Rayleigh–Bénard convection, European Journal of Mechanics - B/Fluids, 72, 164–178, https://doi.org/https://doi.org/10.1016/j.euromechflu.2018.05.007, 2018.

de la Torre Juárez, M., Chavez, A., Tamppari, L. K., Munguira, A., Martínez, G., Hueso, R., Chide, B., Murdoch, N., Stott, A. E., Navarro, S., Sánchez-Lavega, A., Orton, G. S., Viúdez-Moreiras, D., Banfield, D. J., and Rodríguez-Manfredi, J. A.: Diurnal Cycle of Rapid Air Temperature Fluctuations at Jezero Crater: Probability Distributions, Exponential Tails, Scaling, and Intermittency, Journal of Geophysical Research: Planets, 128, e2022JE007 458, https://doi.org/https://doi.org/10.1029/2022JE007458, e2022JE007458 2022JE007458, 2023.

de Wit, X. M., van Kan, A., and Alexakis, A.: Bistability of the large-scale dynamics in quasi-two-dimensional turbulence, Journal of Fluid Mechanics, 939, R2, https://doi.org/10.1017/jfm.2022.209, 2022.

Desai, N., Chandrakar, K. K., Chang, K., Cantrell, W., and Shaw, R. A.: Influence of Microphysical Variability on Stochastic Condensation in a Turbulent Laboratory Cloud, Journal of the Atmospheric Sciences, 75, 189 – 201, https://doi.org/10.1175/JAS-D-17-0158.1, 2018.

Desai, N., Chandrakar, K. K., Kinney, G., Cantrell, W., and Shaw, R. A.: Aerosol-Mediated Glaciation of Mixed-Phase Clouds: Steady-State Laboratory Measurements, Geophysical Research Letters, 46, 9154–9162, https://doi.org/https://doi.org/10.1029/2019GL083503, 2019.

du Puits, R.: Time-resolved measurements of the local wall heat flux in turbulent Rayleigh–Bénard convection, International Journal of Heat and Mass Transfer, 188, 122 649, https://doi.org/https://doi.org/10.1016/j.ijheatmasstransfer.2022.122649, 2022.

du Puits, R.: Thermal boundary layers in turbulent Rayleigh-Bénard convection with rough and smooth plates: A one-to-one comparison, Phys. Rev. Fluids, 9, 023 501, https://doi.org/10.1103/PhysRevFluids.9.023501, 2024.

du Puits, R., Resagk, C., and Thess, A.: Thermal boundary layers in turbulent Rayleigh–Bénard convection at aspect ratios between 1 and 9, New Journal of Physics, 15, 013 040, https://doi.org/10.1088/1367-2630/15/1/013040, 2013.

Eidelman, A., Elperin, T., Gluzman, I., and Golbraikh, E.: Helicity of mean and turbulent flow with coherent structures in Rayleigh-Bénard convective cell, Physics of Fluids, 26, 065 103, https://doi.org/10.1063/1.4881939, 2014.

Fan, Y., Zhao, Y., Torres, J. F., Xu, F., Lei, C., Li, Y., and Carmeliet, J.: Natural convection over vertical and horizontal heated flat surfaces: A review of recent progress focusing on underpinnings and implications for heat transfer and environmental applications, Physics of Fluids, 33, 101 301, https://doi.org/10.1063/5.0065125, 2021.

Fernando, H. and Smith IV, D.: Vortex structures in geophysical convection, European Journal of Mechanics - B/Fluids, 20, 437–470, https://doi.org/https://doi.org/10.1016/S0997-7546(01)01129-3, 2001.

Foroozani, N., Niemela, J. J., Armenio, V., and Sreenivasan, K. R.: Reorientations of the large-scale flow in turbulent convection in a cube, Phys. Rev. E, 95, 033 107, https://doi.org/10.1103/PhysRevE.95.033107, 2017.

Funfschilling, D., Brown, E., and Ahlers, G.: Torsional oscillations of the large-scale circulation in turbulent Rayleigh–Bénard convection, Journal of Fluid Mechanics, 607, 119–139, https://doi.org/10.1017/S0022112008001882, 2008.

Goluskin, D.: Internally Heated Convection and Rayleigh-Bénard Convection, SpringerBriefs in Applied Sciences and Technology, Springer International Publishing, ISBN 9783319239415, https://doi.org/10.1007/978-3-319-23941-5, 2015.

Gotoh, T. and Yeung, P.: Ten Chapters in Turbulence, p. 87–131, Cambridge University Press, https://doi.org/10.1017/CBO9781139032810, 2012.

Guo, S.-X., Zhou, S.-Q., Qu, L., Cen, X.-R., and Lu, Y.-Z.: Evolution and statistics of thermal plumes in tilted turbulent convection, International Journal of Heat and Mass Transfer, 111, 933–942, https://doi.org/https://doi.org/10.1016/j.ijheatmasstransfer.2017.04.039, 2017.

Haman, K. E., Makulski, A., Malinowski, S. P., and Busen, R.: A new ultrafast thermometer for airborne measurements in clouds, Journal of Atmospheric and Oceanic Technology, 14, 217–227, https://doi.org/10.1175/1520-0426(1997)014<0217:ANUTFA>2.0.CO;2, 1997.

Haman, K. E., Malinowski, S. P., and Struś, B. D.: Two new types of ultrafast aircraft thermometer, Journal of Atmospheric and Oceanic Technology, 18, 117–134, https://doi.org/10.1175/1520-0426, 2001.

He, X., van Gils, D. P. M., Bodenschatz, E., and Ahlers, G.: Logarithmic Spatial Variations and Universal f^{-1} Power Spectra of Temperature Fluctuations in Turbulent Rayleigh-Bénard Convection, Phys. Rev. Lett., 112, 174 501, https://doi.org/10.1103/PhysRevLett.112.174501, 2014.

He, X., Wang, Y., and Tong, P.: Dynamic heterogeneity and conditional statistics of non-Gaussian temperature fluctuations in turbulent thermal convection, Phys. Rev. Fluids, 3, 052 401, https://doi.org/10.1103/PhysRevFluids.3.052401, 2018.

He, Y.-H. and Xia, K.-Q.: Temperature Fluctuation Profiles in Turbulent Thermal Convection: A Logarithmic Dependence versus a Power-Law Dependence, Phys. Rev. Lett., 122, 014 503, https://doi.org/10.1103/PhysRevLett.122.014503, 2019.

Khurshid, S., Donzis, D. A., and Sreenivasan, K. R.: Energy spectrum in the dissipation range, Phys. Rev. Fluids, 3, 082 601, https://doi.org/10.1103/PhysRevFluids.3.082601, 2018.

Krug, D., Lohse, D., and Stevens, R. J. A. M.: Coherence of temperature and velocity superstructures in turbulent Rayleigh–Bénard flow, Journal of Fluid Mechanics, 887, A2, https://doi.org/10.1017/jfm.2019.1054, 2020.

Kukharets, V. P. and Nalbandyan, H. G.: Temperature fluctuations in the atmospheric surface layer over the thermally inhomogeneous underlying surface, Izvestiya, Atmospheric and Oceanic Physics, 42, 456–462, https://doi.org/10.1134/S0001433806040050, 2006.

Kumala, W., Haman, K. E., Kopec, M. K., Khelif, D., and Malinowski, S. P.: Modified ultrafast thermometer UFT-M and temperature measurements during Physics of Stratocumulus Top (POST), Atmospheric Measurement Techniques, 6, 2043–2054, https://doi.org/10.5194/amt-6-2043-2013, 2013.

Kumar, A. and Verma, M. K.: Applicability of Taylor's hypothesis in thermally driven turbulence, Royal Society Open Science, 5, 172 152, https://doi.org/10.1098/rsos.172152, 2018.

Lakkaraju, R., Stevens, R. J. A. M., Verzicco, R., Grossmann, S., Prosperetti, A., Sun, C., and Lohse, D.: Spatial distribution of heat flux and fluctuations in turbulent Rayleigh-Bénard convection, Phys. Rev. E, 86, 056 315, https://doi.org/10.1103/PhysRevE.86.056315, 2012.

Lenschow, D. H., Mann, J., and Kristensen, L.: How Long Is Long Enough When Measuring Fluxes and Other Turbulence Statistics?, Journal of Atmospheric and Oceanic Technology, 11, 661–673, https://doi.org/https://doi.org/10.1175/1520-0426(1994)011<0661:HLILEW>2.0.CO;2, 1994.

Liu, Y. and Ecke, R. E.: Local temperature measurements in turbulent rotating Rayleigh-Bénard convection, Phys. Rev. E, 84, 016 311, https://doi.org/10.1103/PhysRevE.84.016311, 2011.

Lohse, D. and Shishkina, O.: Ultimate Rayleigh-Bénard turbulence, Rev. Mod. Phys., 96, 035 001, https://doi.org/10.1103/RevModPhys.96.035001, 2024.

Lohse, D. and Xia, K.-Q.: Small-Scale Properties of Turbulent Rayleigh-Bénard Convection, Annual Review of Fluid Mechanics, 42, 335–364, https://doi.org/https://doi.org/10.1146/annurev.fluid.010908.165152, 2010.

MacMillan, T., Shaw, R. A., Cantrell, W. H., and Richter, D. H.: Direct numerical simulation of turbulence and microphysics in the Pi Chamber, Phys. Rev. Fluids, 7, 020 501, https://doi.org/10.1103/PhysRevFluids.7.020501, 2022.

Mishra, P. K., De, A. K., Verma, M. K., and Eswaran, V.: Dynamics of reorientations and reversals of large-scale flow in Rayleigh–Bénard convection, Journal of Fluid Mechanics, 668, 480–499, https://doi.org/10.1017/S0022112010004830, 2011.

Moller, S., Resagk, C., and Cierpka, C.: Long-time experimental investigation of turbulent superstructures in Rayleigh–Bénard convection by noninvasive simultaneous measurements of temperature and velocity fields, Experiments in Fluids, 62, 64, https://doi.org/10.1007/s00348-020-03107-1, 2021.

Musacchio, S. and Boffetta, G.: Condensate in quasi-two-dimensional turbulence, Phys. Rev. Fluids, 4, 022 602, https://doi.org/10.1103/PhysRevFluids.4.022602, 2019.

Niedermeier, D., Chang, K., Cantrell, W., Chandrakar, K. K., Ciochetto, D., and Shaw, R. A.: Observation of a link between energy dissipation rate and oscillation frequency of the large-scale circulation in dry and moist Rayleigh-Bénard turbulence, Phys. Rev. Fluids, 3, 083 501, https://doi.org/10.1103/PhysRevFluids.3.083501, 2018.

Niemela, J. J., Skrbek, L., Sreenivasan, K. R., and Donnelly, R. J.: Turbulent convection at very high Rayleigh numbers, Nature, 404, 837–840, https://doi.org/10.1038/35009036, 2000.

Nowak, J., Kumala, W., Kwiatkowski, A., Kwiatkowski, K., Czyżewska, D., Karpińska, K., and Malinowski, S.: UltraFast Thermometer 2.0 - new temperature sensor for airborne applications and its performance during ACORES 2017, Geophysical Research Abstracts, https://doi.org/10.13140/RG.2.2.12500.24967, 2018.

Nowak, J. L., Siebert, H., Szodry, K.-E., and Malinowski, S. P.: Coupled and decoupled stratocumulus-topped boundary layers: turbulence properties, Atmospheric Chemistry and Physics Discussions, 2021, 1–41, https://doi.org/10.5194/acp-2021-214, 2021.

Olsthoorn, J.: Accounting for surface temperature variations in Rayleigh-Bénard convection, Phys. Rev. Fluids, 8, 033 501, https://doi.org/10.1103/PhysRevFluids.8.033501, 2023.

Pandey, A., Scheel, J. D., and Schumacher, J.: Turbulent superstructures in Rayleigh-Bénard convection, Nature Communications, 9, 2118, https://doi.org/10.1038/s41467-018-04478-0, 2018.

Pawar, S. S. and Arakeri, J. H.: Kinetic energy and scalar spectra in high Rayleigh number axially homogeneous buoyancy driven turbulence, Physics of Fluids, 28, 065 103, https://doi.org/10.1063/1.4953858, 2016.

Plunian, F., Teimurazov, A., Stepanov, R., and Verma, M. K.: Inverse cascade of energy in helical turbulence, Journal of Fluid Mechanics, 895, A13, https://doi.org/10.1017/jfm.2020.307, 2020.

Prabhakaran, P., Shawon, A. S. M., Kinney, G., Thomas, S., Cantrell, W., and Shaw, R. A.: The role of turbulent fluctuations in aerosol activation and cloud formation, Proceedings of the National Academy of Sciences, 117, 16 831–16 838, https://doi.org/10.1073/pnas.2006426117, 2020.

Reiter, P., Shishkina, O., Lohse, D., and Krug, D.: Crossover of the relative heat transport contributions of plume ejecting and impacting zones in turbulent Rayleigh-Bénard convection(a), Europhysics Letters, 134, 34 002, https://doi.org/10.1209/0295-5075/134/34002, 2021.

Rieutord, M., Roudier, T., Rincon, F., Malherbe, J.-M., Meunier, N., Berger, T., and Frank, Z.: On the power spectrum of solar surface flows, A&A, 512, A4, https://doi.org/10.1051/0004-6361/200913303, 2010.

Sakievich, P., Peet, Y., and Adrian, R.: Large-scale thermal motions of turbulent Rayleigh–Bénard convection in a wide aspect-ratio cylindrical domain, International Journal of Heat and Fluid Flow, 61, https://doi.org/10.1016/j.ijheatfluidflow.2016.04.011, 2016.

Salesky, S. T., Gillis, K., Anderson, J., Helman, I., Cantrell, W., and Shaw, R. A.: Modeling the subgrid scale scalar variance: a priori tests and application to supersaturation in cloud turbulence, Journal of the Atmospheric Sciences, https://doi.org/10.1175/JAS-D-23-0163.1, 2024.

Shevkar, P. P., Vishnu, R., Mohanan, S. K., Koothur, V., Mathur, M., and Puthenveettil, B. A.: On separating plumes from boundary layers in turbulent convection, Journal of Fluid Mechanics, 941, A5, https://doi.org/DOI: 10.1017/jfm.2022.271, 2022.

Shi, N., Emran, M. S., and Schumacher, J.: Boundary layer structure in turbulent Rayleigh–Bénard convection, Journal of Fluid Mechanics, 706, 5–33, https://doi.org/DOI: 10.1017/jfm.2012.207, 2012.

Shishkina, O.: Rayleigh-Bénard convection: The container shape matters, Phys. Rev. Fluids, 6, 090 502, https://doi.org/10.1103/PhysRevFluids.6.090502, 2021.

Shishkina, O., Horn, S., Emran, M. S., and Ching, E. S. C.: Mean temperature profiles in turbulent thermal convection, Phys. Rev. Fluids, 2, 113 502, https://doi.org/10.1103/PhysRevFluids.2.113502, 2017.

Siebert, H., Lehmann, K., and Wendisch, M.: Observations of small-scale turbulence and energy dissipation rates in the cloudy boundary layer, Journal of the Atmospheric Sciences, 63, 1451–1466, https://doi.org/10.1175/JAS3687.1, 2006.

Siebert, H., Szodry, K. E., Egerer, U., Wehner, B., Henning, S., Chevalier, K., Lückerath, J., Welz, O., Weinhold, K., Lauermann, F., Gottschalk, M., Ehrlich, A., Wendisch, M., Fialho, P., Roberts, G., Allwayin, N., Schum, S., Shaw, R. A., Mazzoleni, C., Mazzoleni, L., Nowak, J. L., Malinowski, S. P., Karpinska, K., Kumala, W., Czyzewska, D., Luke, E. P., Kollias, P., Wood, R., and Mellado, J. P.: Observations of aerosol, cloud, turbulence, and radiation properties at the top of the Marine Boundary Layer over the Eastern North Atlantic Ocean: The ACORES Campaign, Bulletin of the American Meteorological Society, 102, E123–E147, https://doi.org/10.1175/BAMS-D-19-0191.1, 2021.

Sreenivasan, K. R.: Turbulent mixing: A perspective, Proceedings of the National Academy of Sciences, 116, 18 175–18 183, https://doi.org/10.1073/pnas.1800463115, 2019.

Stevens, B., Bony, S., Farrell, D., Ament, F., Blyth, A., Fairall, C., Karstensen, J., Quinn, P. K., Speich, S., Acquistapace, C., Aemisegger, F., Albright, A. L., Bellenger, H., Bodenschatz, E., Caesar, K. A., Chewitt-Lucas, R., De Boer, G., Delanoë, J., Denby, L., Ewald, F., Fildier, B., Forde, M., George, G., Gross, S., Hagen, M., Hausold, A., Heywood, K. J., Hirsch, L., Jacob, M., Jansen, F., Kinne, S., Klocke, D., Kölling, T., Konow, H., Lothon, M., Mohr, W., Naumann, A. K., Nuijens, L., Olivier, L., Pincus, R., Pöhlker, M., Reverdin, G., Roberts, G., Schnitt, S., Schulz, H., Pier Siebesma, A., Stephan, C. C., Sullivan, P., Touzé-Peiffer, L., Vial, J., Vogel, R., Zuidema, P., Alexander, N., Alves, L., Arixi, S., Asmath, H., Bagheri, G., Baier, K., Bailey, A., Baranowski, D., Baron, A., Barrau, S., Barrett, P. A., Batier, F., Behrendt, A., Bendinger, A., Beucher, F., Bigorre, S., Blades, E., Blossey, P., Bock, O., Böing, S., Bosser, P., Bourras, D., Bouruet-Aubertot, P., Bower, K., Branellec, P., Branger, H., Brennek, M., Brewer, A., Brilouet, P. E., Brügmann, B., Buehler, S. A., Burke, E., Burton, R., Calmer, R., Canonici, J. C., Carton, X., Cato, G., Charles, J. A., Chazette, P., Chen, Y., Chilinski, M. T., Choularton, T., Chuang, P., Clarke, S., Coe, H., Cornet, C., Coutris, P., Couvreux, F., Crewell, S., Cronin, T., Cui, Z., Cuypers, Y., Daley, A., Damerell, G. M., Dauhut, T., Deneke, H., Desbios, J. P., Dörner, S., Donner, S., Douet, V., Drushka, K., Dütsch, M., Ehrlich, A., Emanuel, K., Emmanouilidis, A., Etienne, J. C., Etienne-Leblanc, S., Faure, G., Feingold, G., Ferrero, L., Fix, A., Flamant, C., Flatau, P. J., Foltz, G. R., Forster, L., Furtuna, I., Gadian, A., Galewsky, J., Gallagher, M., Gallimore, P., Gaston, C., Gentemann, C., Geyskens, N., Giez, A., Gollop, J., Gouirand, I., Gourbeyre, C., De Graaf, D., De Groot, G. E., Grosz, R., Güttler, J., Gutleben, M., Hall, K., Harris, G., Helfer, K. C., Henze, D., Herbert, C., Holanda, B., Ibanez-Landeta, A., Intrieri, J., Iyer, S., Julien, F., Kalesse, H., Kazil, J., Kellman, A., Kidane, A. T., Kirchner, U., Klingebiel, M., Körner, M., Kremper, L. A., Kretzschmar, J., Krüger, O., Kumala, W., Kurz, A., L'Hégaret, P., Labaste, M., Lachlan-Cope, T., Laing, A., Landschützer, P., Lang, T., Lange, D., Lange, I., Laplace, C., Lavik, G., Laxenaire, R., LeBihan, C., Leandro, M., Lefevre, N., Lena, M., Lenschow, D., Li, Q., Lloyd, G., Los, S., Losi, N., Lovell, O., Luneau, C., Makuch, P., Malinowski, S., Manta, G., Marinou, E., Marsden, N., Masson, S., Maury, N., Mayer, B., Mayers-Als, M., Mazel, C., McGeary, W., McWilliams, J. C., Mech, M., Mehlmann, M., Meroni, A. N., Mieslinger, T., Minikin, A., Minnett, P., Möller, G., Avalos, Y. M., Muller, C., Musat, I., Napoli, A., Neuberger, A., Noisel, C., Noone, D., Nordsiek, F., Nowak, J. L., Oswald, L., Parker, D. J., Peck, C., Person, R., Philippi, M., Plueddemann, A., Pöhlker, C., Pörtge, V., Pöschl, U., Pologne, L., Posyniak, M., Prange, M., Meléndez, E. Q., Radtke, J., Ramage, K., Reimann, J., Renault, L., Reus, K., Reyes, A., Ribbe, J., Ringel, M., Ritschel, M., Rocha, C. B., Rochetin, N., Röttenbacher, J., Rollo, C., Royer, H., Sadoulet, P., Saffin, L., Sandiford, S., Sandu, I., Schäfer, M., Schemann, V., Schirmacher, I., Schlenczek, O., Schmidt, J., Schröder, M., Schwarzenboeck, A., Sealy, A., Senff, C. J., Serikov, I., Shohan, S., Siddle, E., Smirnov, A., Späth, F., Spooner, B., Katharina Stolla, M., Szkólka, W., De Szoeke, S. P., Tarot, S., Tetoni, E., Thompson, E., Thomson, J., Tomassini, L., Totems, J., Ubele, A. A., Villiger, L., Von Arx, J., Wagner, T., Walther, A., Webber, B., Wendisch, M., Whitehall, S., Wiltshire, A., Wing, A. A., Wirth, M., Wiskandt, J., Wolf, K., Worbes, L., Wright, E., Wulfmeyer, V., Young, S., Zhang, C., Zhang, D., Ziemen, F., Zinner, T., and Zöger, M.: EUREC4A, Earth System Science Data, 13, 4067–4119, https://doi.org/10.5194/ESSD-13-4067-2021, 2021.

Stevens, R. J. A. M., Blass, A., Zhu, X., Verzicco, R., and Lohse, D.: Turbulent thermal superstructures in Rayleigh-Bénard convection, Phys. Rev. Fluids, 3, 041 501, https://doi.org/10.1103/PhysRevFluids.3.041501, 2018.

van der Poel, E. P., Ostilla-Mónico, R., Verzicco, R., Grossmann, S., and Lohse, D.: Logarithmic Mean Temperature Profiles and Their Connection to Plume Emissions in Turbulent Rayleigh-Bénard Convection, Phys. Rev. Lett., 115, 154 501, https://doi.org/10.1103/PhysRevLett.115.154501, 2015.

Vasiliev, A., Sukhanovskii, A., Frick, P., Budnikov, A., Fomichev, V., Bolshukhin, M., and Romanov, R.: High Rayleigh number convection in a cubic cell with adiabatic sidewalls, International Journal of Heat and Mass Transfer, 102, 201–212, https://doi.org/https://doi.org/10.1016/j.ijheatmasstransfer.2016.06.015, 2016.

Vishnu, V. T., De, A. K., and Mishra, P. K.: Dynamics of large-scale circulation and energy transfer mechanism in turbulent Rayleigh–Bénard convection in a cubic cell, Physics of Fluids, 32, 095 115, https://doi.org/10.1063/5.0021667, 2020.

Vishnu, V. T., De, A. K., and Mishra, P. K.: Statistics of thermal plumes and dissipation rates in turbulent Rayleigh-Bénard convection in a cubic cell, International Journal of Heat and Mass Transfer, 182, 121 995, https://doi.org/https://doi.org/10.1016/j.ijheatmasstransfer.2021.121995, 2022.

Wagner, S., Shishkina, O., and Wagner, C.: Boundary layers and wind in cylindrical Rayleigh–Bénard cells, Journal of Fluid Mechanics, 697, 336–366, 2012.

Wang, Q., Xia, S.-N., Wang, B.-F., Sun, D.-J., Zhou, Q., and Wan, Z.-H.: Flow reversals in two-dimensional thermal convection in tilted cells, Journal of Fluid Mechanics, 849, 355–372, https://doi.org/10.1017/jfm.2018.451, 2018.

Wang, Y., He, X., and Tong, P.: Turbulent temperature fluctuations in a closed Rayleigh–Bénard convection cell, Journal of Fluid Mechanics, 874, 263–284, https://doi.org/10.1017/jfm.2019.405, 2019.

Wang, Y., Wei, Y., Tong, P., and He, X.: Collective effect of thermal plumes on temperature fluctuations in a closed Rayleigh–Bénard convection cell, Journal of Fluid Mechanics, 934, A13, https://doi.org/10.1017/jfm.2021.1107, 2022.

Wei, P.: The persistence of large-scale circulation in Rayleigh–Bénard convection, Journal of Fluid Mechanics, 924, A28, https://doi.org/10.1017/jfm.2021.619, 2021.

Xi, H.-D., Lam, S., and Xia, K.-Q.: From laminar plumes to organized flows: the onset of large-scale circulation in turbulent thermal convection, Journal of Fluid Mechanics, 503, 47–56, https://doi.org/10.1017/S0022112004008079, 2004.

Xi, H.-D., Zhou, S.-Q., Zhou, Q., Chan, T.-S., and Xia, K.-Q.: Origin of the Temperature Oscillation in Turbulent Thermal Convection, Phys. Rev. Lett., 102, 044 503, https://doi.org/10.1103/PhysRevLett.102.044503, 2009.

Xu, A., Chen, X., and Xi, H.-D.: Tristable flow states and reversal of the large-scale circulation in two-dimensional circular convection cells, Journal of Fluid Mechanics, 910, A33, https://doi.org/10.1017/jfm.2020.964, 2021a.

Xu, W., Wang, Y., He, X., Wang, X., Schumacher, J., Huang, S.-D., and Tong, P.: Mean velocity and temperature profiles in turbulent Rayleigh–Bénard convection at low Prandtl numbers, Journal of Fluid Mechanics, 918, A1, https://doi.org/10.1017/jfm.2021.255, 2021b.

Yan, Z., Li, X., and Yu, C.: Scale locality of helicity cascade in physical space, Physics of Fluids, 32, 061 705, https://doi.org/10.1063/5.0013009, 2020.

Yano, J.: Geophysical Convection Dynamics, no. t. 5 in Developments in Weather and Climate Science, Elsevier Science, ISBN 9780323912136, https://books.google.pl/books?id=bmG9EAAAQBAJ, 2023.

Yano, J.-I. and Morrison, H.: Thermal vortex ring: vortex-dynamics analysis of a high-resolution simulation, Journal of Fluid Mechanics, 991, A18, https://doi.org/10.1017/jfm.2024.485, 2024.

Yao, J. and Hussain, F.: Vortex Reconnection and Turbulence Cascade, Annual Review of Fluid Mechanics, 54, 317–347, https://doi.org/10.1146/annurev-fluid-030121-125143, 2022.

Zhang, Y.-Z., Sun, C., Bao, Y., and Zhou, Q.: How surface roughness reduces heat transport for small roughness heights in turbulent Rayleigh–Bénard convection, Journal of Fluid Mechanics, 836, https://doi.org/10.1017/jfm.2017.786, 2018.

Zhou, Q. and Xia, K.-Q.: Thermal boundary layer structure in turbulent Rayleigh–Bénard convection in a rectangular cell, Journal of Fluid Mechanics, 721, 199–224, https://doi.org/10.1017/jfm.2013.73, 2013.

Zhou, S.-Q. and Xia, K.-Q.: Scaling Properties of the Temperature Field in Convective Turbulence, Phys. Rev. Lett., 87, 064 501, https://doi.org/10.1103/PhysRevLett.87.064501, 2001.

Zhou, S.-Q., Xie, Y.-C., Sun, C., and Xia, K.-Q.: Statistical characterization of thermal plumes in turbulent thermal convection, Phys. Rev. Fluids, 1, 054 301, https://doi.org/10.1103/PhysRevFluids.1.054301, 2016.

Zhu, X., Mathai, V., Stevens, R. J. A. M., Verzicco, R., and Lohse, D.: Transition to the Ultimate Regime in Two-Dimensional Rayleigh-Bénard Convection, Phys. Rev. Lett., 120, 144 502, https://doi.org/10.1103/PhysRevLett.120.144502, 2018.

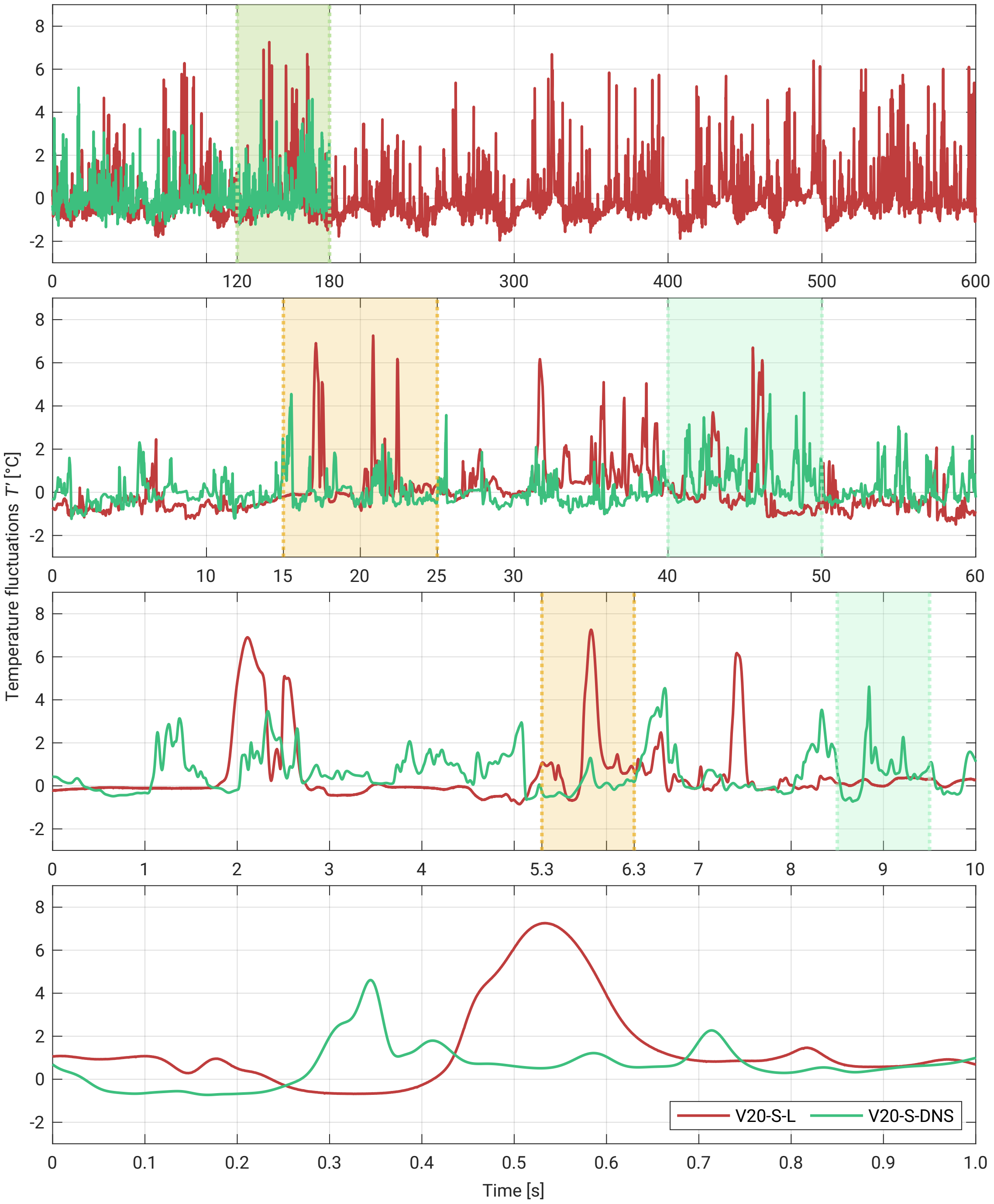

Figure A1. Experimental versus DNS T' series $\sim$8 cm above the floor showed in the following zoomed in time segments: 600 s, 60 s, 10 s, and 1 s. The used dataset covers $\Delta T = 20$ K case. Please note that the time series from the experiment and the DNS simulation do not correspond to each other.

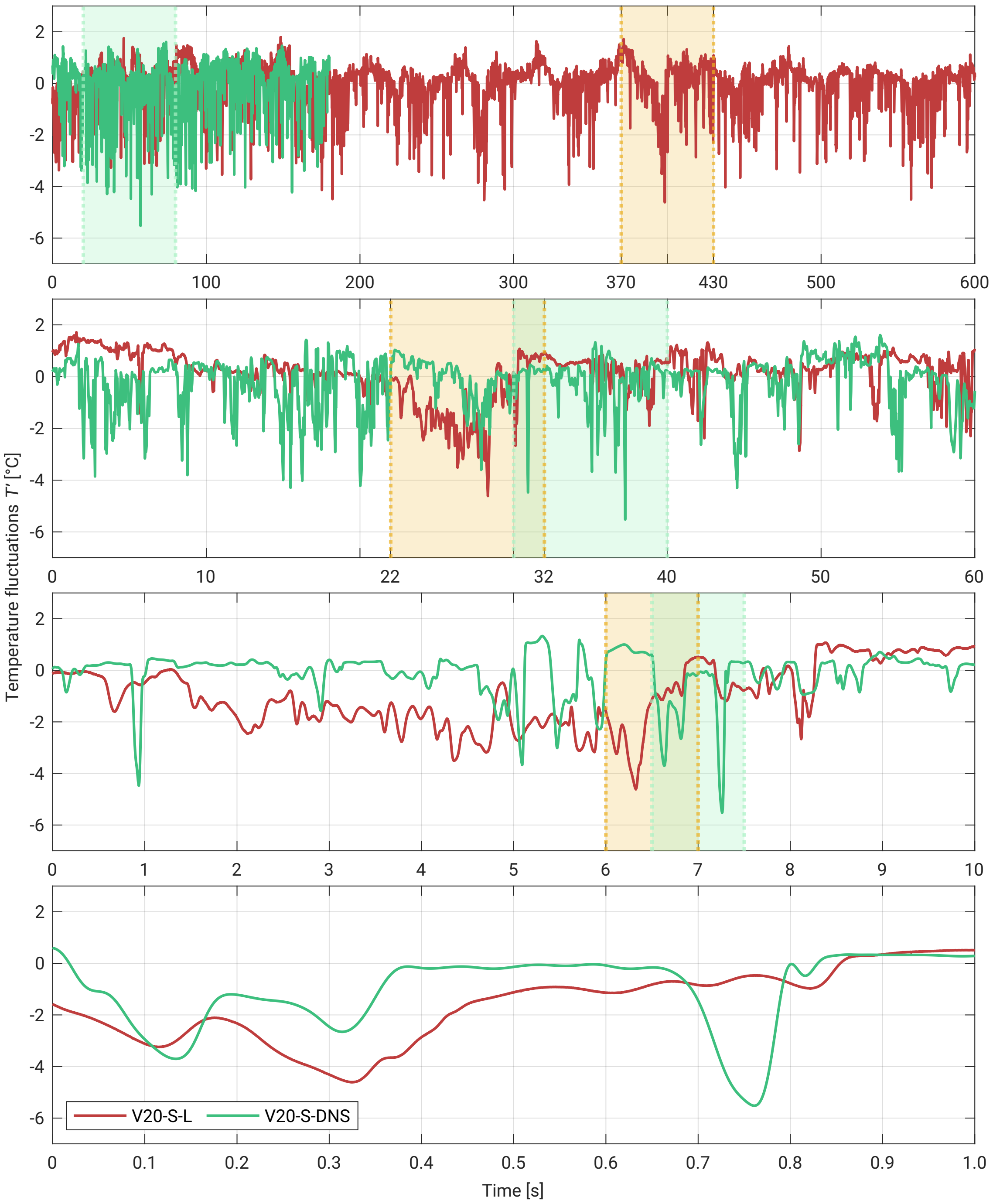

Figure A2. Experimental versus DNS T' series $\sim$5 cm below the ceiling showed in the following zoomed in time segments: 600 s, 60 s, 10 s, and 1 s. The used dataset covers $\Delta T = 20$ K case. Please note that the time series from the experiment and the DNS simulation do not correspond to each other.

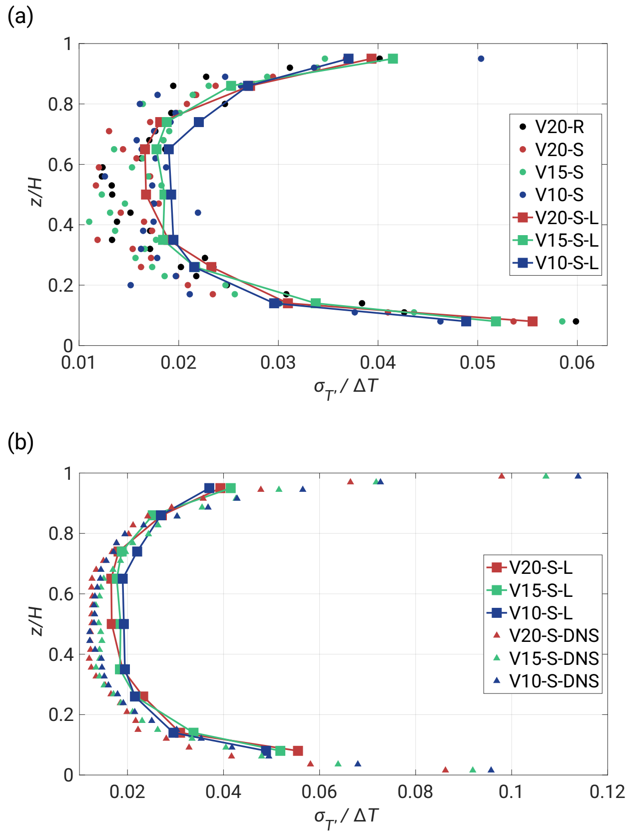

Figure B1. Non-dimensionalized standard deviation scaled by corresponding ΔT. In the figure z/H represents vertical distance z measured from the bottom plate being normalized by the cell height $H = 1$ m. **(a)** Analogy of Fig. 5. **(b)** Analogy of Fig. 11.

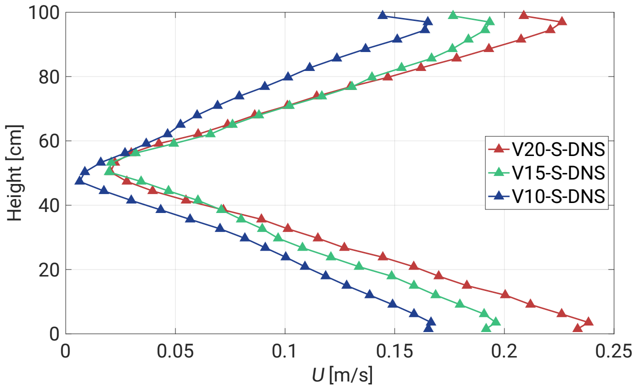

Figure C1. Magnitude of the mean velocity U profile near the axis of the chamber with respect to its height. Each curve represent different ΔT.

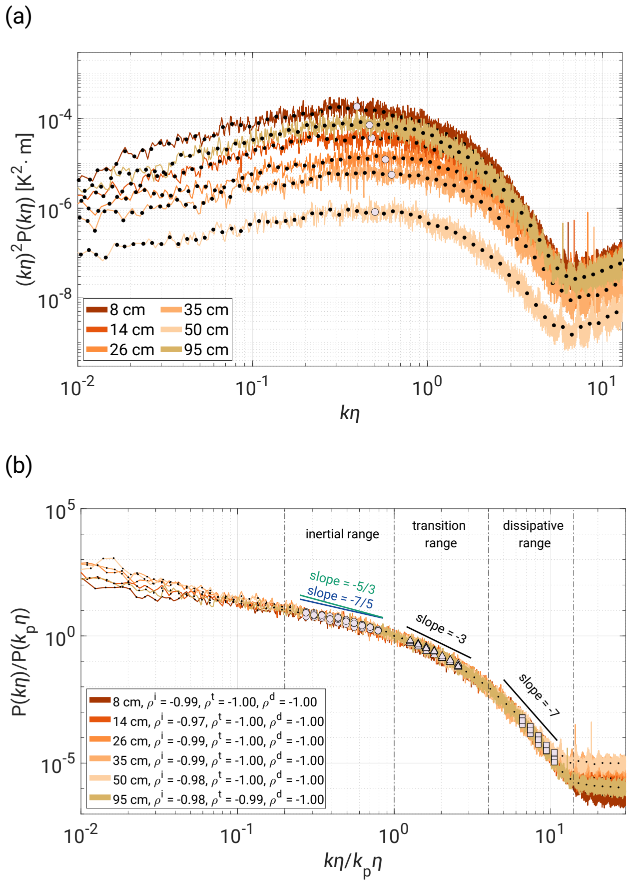

Figure C2. Analogical to Fig. 8 spectra of V20-S-L case but in wavenumber domain. **(a)** Scaled spectrum of $k\eta^2 P(k\eta)$. **(b)** PSD $P(k\eta)/P(k_\mathrm{p}\eta)$ versus $k\eta/k_\mathrm{p}\eta$ with three defined regimes: inertial range (circles, $0.2 \leqslant k\eta/k_\mathrm{p}\eta \leqslant 1$), transition range (triangles, $1 \leqslant k\eta/k_\mathrm{p}\eta \leqslant 4$), and dissipative range (squares, $4 \leqslant k\eta/k_\mathrm{p}\eta \leqslant 20$). Legend includes the Pearson correlation coefficients p.

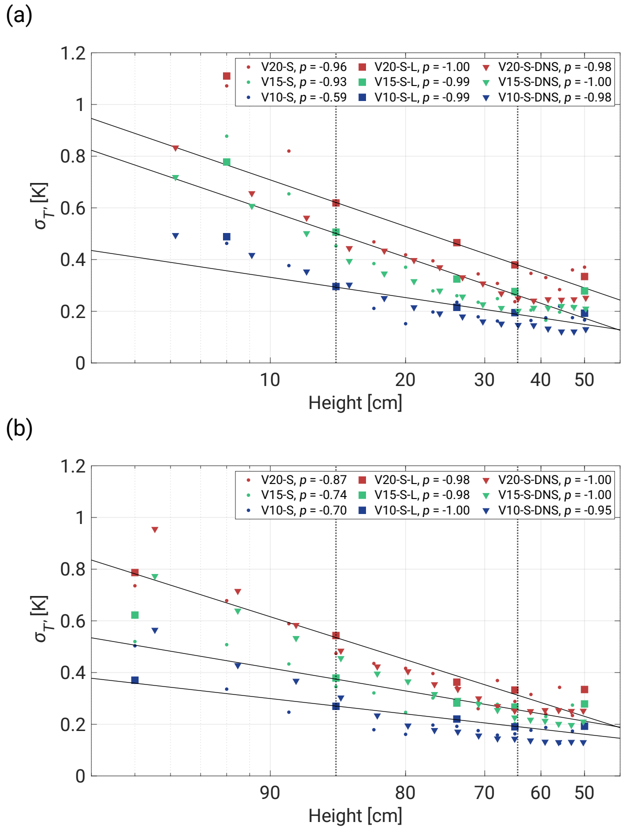

Figure D1. Standard deviation $\sigma_{T'}$ distribution of both 19 min, 3 min and DNS dataset in semi-log domain near the floor **(a)** and close to the ceiling **(b)**. Both legends include Pearson correlation coefficients. Note that the fitted curves correspond only with 19 min measurements.